Received: 27 April 2022 | Revised: 12 September 2022 | Accepted: 26 September 2022 | Published on: 4 November 2022

DOI: 10.1002/qj.4374

Quarterly Journal of the Royal Meteorological Society RMetS

RESEARCH ARTICLE

Modeling cloud properties over the 79 N Glacier (Nioghalvfjerdsfjorden, NE Greenland) for an intense summer melt period in 2019

Malena Andernach[1] | **Jenny V. Turton**[1] | **Thomas Mölg**[1]

[1]Climate System Research Group, Institute of Geography, Friedrich-Alexander University (FAU), Erlangen, Germany

Correspondence
Malena Andernach, International Max Planck Research School on Earth System Modelling, Max Planck Institute for Meteorology, 20146 Hamburg, Germany.
Email: malena.andernach@mpimet.mpg.de

Present Address
Malena Andernach, Max Planck Institute for Meteorology, 20146 Hamburg, Germany.

Jenny V. Turton, Arctic Frontiers AS, 9007 Tromsø, Norway

Funding information
German Federal Ministry for Education and Research, Grant/Award Number: 03F0855D

Abstract

Long believed to be insignificant, melt activity on the Northeast Greenland Ice Stream (NEGIS) has increased in recent years. Summertime Arctic clouds have the potential to strongly affect surface melt processes by regulating the amount of radiation received at the surface. However, the cloud effect over Greenland is spatially and temporally variable and high-resolution information on the northeast is absent. This study aims at exploring the potential of a high-resolution configuration of the polar-optimized Weather Research & Forecasting Model (PWRF) in simulating cloud properties in the area of the Nioghalvfjerdsfjorden Glacier (79 N Glacier). Subsequently, the model simulations are employed to investigate the impact of Arctic clouds on the surface energy budget and on surface melting during the extensive melt event at the end of July 2019. Compared to automatic weather station (AWS) measurements and remote-sensing data (Sentinel-2A and the Moderate Resolution Imaging Spectroradiometer, MODIS), PWRF simulates cloud properties with sufficient accuracy. It appears that peak melt was caused by an increase in solar radiation and sensible heat flux (SHF) in response to a blocking anticyclone and foehn winds in the absence of clouds. Cloud warming over high-albedo surfaces helped to precondition the surface and prolonged the melting as the anticyclone abated. The results are sensitive to the surface albedo and suggest spatiotemporal differences in the cloud effect as snow and ice properties change over the course of the melting season. This demonstrates the importance of including high-resolution information on clouds in analyses of ice sheet dynamics.

KEYWORD

cloud properties, cloud radiative effect, Northeast Greenland Ice Stream, regional climate modeling, surface energy balance, surface melt

1 | INTRODUCTION

In the Arctic, temperatures have risen at almost four times the global mean rate in recent decades (Rantanen *et al.*, 2022), a phenomenon referred to as Arctic amplification (Manabe and Stouffer, 1980; Lee *et al.*, 2021). Together with temperature rise, the mass balance of the Greenland Ice Sheet (GrIS) has transitioned from a positive (mass gain) or near equilibrium state before the 1990s to a negative state (mass loss) in the 20th century (e.g., Mouginot *et al.*, 2019). In the 21st century, mass loss of the GrIS has even accelerated (e.g., van den Broeke *et al.*, 2016; The IMBIE Team, 2020), resulting in a cumulative ice loss of approximately 3,902 Gt during 1992 and 2018 and a global sea-level rise contribution of 10.6 mm (The IMBIE Team, 2020).

The acceleration of the 21st century mass loss is characterized by substantial interannual variability (van den Broeke *et al.*, 2017). The beginning of the century was marked by a couple of major melt events with, 2002, 2010, 2012 and 2019 standing out (van As *et al.*, 2012; Hall *et al.*, 2013; Tedesco and Fettweis, 2020). During the unprecedented melt event in July 2012, almost the entire ice sheet experienced surface melt (Nghiem *et al.*, 2012; Hall *et al.*, 2013), including at Summit Station, which is over 3,000 m a.s.l. (Nghiem *et al.*, 2012). Ice-core records from the same location revealed the rarity of such events, with the last occurring in 1889 (Clausen *et al.*, 1988). However, a series of cold summers, especially in the west and increased snowfall in the east (Zhang *et al.*, 2019; Sasgen *et al.*, 2020), recently slowed down the total rate of mass loss (The IMBIE Team, 2020). This phase of reduced ice loss is interrupted by a record melt year in 2019 with an annual mass loss of 532 Gt revealed by satellite measurements (Sasgen *et al.*, 2020). Although total June–August (JJA) runoff was lower than in 2012, the surface mass balance was the lowest on record, and Summit Station experienced melting again (Tedesco and Fettweis, 2020). In August 2021, even the first rainfall event was reported at Summit Station (Moon *et al.*, 2021).

For decades, the highest melt has occurred in southern regions (Rignot and Kanagaratnam, 2006; Velicogna and Wahr, 2006). However, in the last decade, accelerated mass loss and highest melt anomalies have been observed in the north, particularly in the northeast (e.g., Hall *et al.*, 2013; Khan *et al.*, 2014; Mouginot *et al.*, 2015; Mouginot *et al.*, 2019). During the anomalous melt in July/August 2019, the Northeast Greenland Ice Stream (NEGIS) mass loss accounted for a fraction of 35%, whereas the southwest participated by around 44% less than in 2012 (Cullather *et al.*, 2020).

With a catchment area of more than 200,000 km^2, the NEGIS is a prominent feature of the GrIS (Rignot and Kanagaratnam, 2006). It drains into the ocean through three marine-terminating outlet glaciers: Zachariæ Isstrøm, Storstrømmen Glacier and Nioghalvfjerdsfjorden Glacier (hereafter abbreviated as 79 N after its latitudinal position), holding a sea-level rise equivalent of 1.1 m in their marine-based sectors (Mouginot *et al.*, 2015). Draining approximately 8% (Rignot and Kanagaratnam, 2006) of the GrIS, 79 N is the largest discharger of ice in northern Greenland. Both the Zachariæ Isstrøm and the 79 N, have accelerated and retreated significantly in recent years, ending their state of relative stability (Khan *et al.*, 2014). Since 1999, the area of the Zachariæ Isstrøm ice shelf shrank by 95% and its flow velocity tripled after the collapse of its floating ice tongue in late 2012 to early 2013 (Mouginot *et al.*, 2015). While mass losses of 79 N have been significantly lower (Andersen *et al.*, 2019), an area of more than 100 km^2 was lost through calving at its outlet in 2019/2020 (Turton *et al.*, 2021). The trend in ice dynamics is attributed to a loss of buttressing sea ice at the ice sheet margin (An *et al.*, 2021) due to the warming of ocean and air temperatures (Sneed and Hamilton, 2016; Turton *et al.*, 2019). Besides ice discharge, enhanced surface melt and runoff have driven ice losses (An *et al.*, 2021; Blau *et al.*, 2021).

Clouds play a pivotal, but sometimes opposing, role in controlling the Arctic surface energy balance (van Tricht *et al.*, 2016; Hofer *et al.*, 2017; Wang *et al.*, 2018; Niwano *et al.*, 2019). They can either warm the surface by trapping and emitting long-wave radiation or cool it by reducing the incident solar radiation (Curry *et al.*, 1996). The extreme dryness of the atmosphere in the Arctic with low clear-sky emissivity enhances the contrast of clouds' greenhouse effects between clear and cloudy states (Curry *et al.*, 1996; Shupe and Intrieri, 2004; Cox *et al.*, 2015). Many major melt events of the GrIS in recent years are associated with cloud dynamics (Bennartz *et al.*, 2013; Hofer *et al.*, 2017; Solomon *et al.*, 2017). It is even suggested that melting would not have occurred at Summit Station during the 2012 melt event without the presence of a cloud cover (Bennartz *et al.*, 2013). The cooling effect of Arctic clouds relies on their ability to scatter incoming solar radiation, so that less energy is available for warming the surface and melting overlying snow or ice layers (Curry *et al.*, 1996; Shupe and Intrieri, 2004). Therefore, an absence of clouds can accelerate surface melt (Hofer *et al.*, 2017; Ruan *et al.*, 2019). Recent studies highlighted the variability of Greenlandic cloud forcing, which is spatially and temporally heterogeneous (Wang *et al.*, 2018; Wang *et al.*, 2019; Izeboud *et al.*, 2020). Important influencing factors can be variations in the surface albedo and the solar zenith angle (SZA) (Minnett, 1999; Shupe and Intrieri, 2004; Wang *et al.*, 2018). Clouds trigger surface melt by long-wave warming predominantly in the highly reflective

accumulation zone, while clouds in the darker ablation zone rather promote short cooling (Wang *et al.*, 2019; Izeboud *et al.*, 2020). However, local and regional effects deviate from the general cloud trend and the magnitude of the cloud effect also depends on cloud phase (Shupe and Intrieri, 2004; Bennartz *et al.*, 2013). It is therefore not possible to generalize the impact of clouds on GrIS surface conditions and high-resolution local-scale studies are required to evaluate their distinct spatiotemporal influence.

Even though Arctic clouds have been identified as decisive in modulating near-surface conditions (Bennartz *et al.*, 2013; van Tricht *et al.*, 2016; Hofer *et al.*, 2017), their exact influence remains uncertain. Given this large uncertainty, they are still only poorly represented in climate models (Lacour *et al.*, 2018; Sedlar *et al.*, 2020; Inoue *et al.*, 2021). While the representation of clouds has been substantially improved in the sixth phase of the Coupled Model Intercomparison Project (CMIP6) compared to CMIP5, the Sixth Assessment Report (AR6) of the IPCC (Intergovernmental Panel on Climate Change) still identified clouds as main contributor to overall uncertainty in climate (Forster *et al.*, 2021). In view of Greenland′s large contribution to global sea-level rise (Oppenheimer *et al.*, 2019) and manifold feedback mechanisms with, for example, ocean circulation (Golledge *et al.*, 2019), it is paramount to understand the role of Arctic clouds as drivers of the GrIS mass loss.

Most of the previous studies analyzing the near-surface impact of Arctic clouds covered the whole Arctic region at a low spatial resolution (e.g., Cesana *et al.*, 2012; Cox *et al.*, 2015; Kay *et al.*, 2016; Hines and Bromwich, 2017; Cho *et al.*, 2020) or the whole of Greenland (e.g., van Tricht *et al.*, 2016; Hofer *et al.*, 2017; Lacour *et al.*, 2018; Niwano *et al.*, 2019; Hahn *et al.*, 2020; Lenaerts *et al.*, 2020), impeding the ability to draw reliable conclusions on smaller regions or single locations. Many of the more small-scale studies focused either on the southeast (Djoumna *et al.*, 2021), the west (van den Broeke *et al.*, 2008; Izeboud *et al.*, 2020; Djoumna *et al.*, 2021) or the interior (i.e., Summit Station; Lacour *et al.*, 2018; Miller *et al.*, 2015; Solomon *et al.*, 2017). Given the large spatial variability in cloud forcing on near-surface conditions (Wang *et al.*, 2019) and the disparate findings, directly transferring their results to other regions such as the NEGIS is not appropriate. However, the increasing contribution of the northeast to GrIS mass losses (Mouginot *et al.*, 2015) necessitates the need to understand the impact clouds have in this region. Until now, little is known about cloud radiative impacts in this region, hampering accurate future mass balance and climate simulations (Flato *et al.*, 2013). Moreover, adequate analysis of the interactions between the NEGIS (i.e., 79 N) and the atmosphere is still missing (Turton *et al.*, 2019).

Greenland′s remote and challenging working environment impedes fieldwork. Consequently, ground observations are only sparsely distributed over the island. A solution to this problem is state-of-the-art models. Previously, the polar-optimized Weather Research & Forecasting Model (PWRF) has been successfully used for modeling more general atmospheric processes in the NEGIS region (Turton *et al.*, 2019; Turton *et al.*, 2020; Turton *et al.*, 2021) as well as for studying polar clouds elsewhere (Listowski and Lachlan-Cope, 2017; Cho *et al.*, 2020). However, no high-resolution study had systematically investigated cloud properties and their role on the near-surface climate conditions of the 79 N area. The overarching research objective of the present study is, thus, to evaluate PWRF′s capability of simulating cloud properties over northeast Greenland. Associated, we assess the effects of Arctic cloud dynamics on the near-surface climate conditions in the area of the 79 N and constrain their impact on surface melt during a case study of an extreme melt event at the end of July and the beginning of August 2019.

2 | DATA AND METHODS

2.1 | Description of the synoptic conditions

Surface mass balance anomalies were record low in the hydrological year September 2018–August 2019 relative to 1981–2010 (Tedesco and Fettweis, 2020). The melt season in 2019 was marked by unusually persistent anticyclonic conditions over the GrIS, that coincided with a negative North Atlantic Oscillation (NAO) index, which was seventh-lowest in the 1950–2019 record, a strongly positive East Atlantic (EA) index and a peaking Greenland Blocking Index (GBI) (Cullather *et al.*, 2020). Cloud dissipation due to anticyclonic conditions enhanced surface melting, which darkened the surface, leading to enhanced melt–albedo feedback. Further, it paved the way for a northward advection of moist, warm air along the western flank (Tedesco and Fettweis, 2020). While fresh snow reflects most of the sunlight due to its high reflectivity, the reduced summer snowfall at that time did not fully cover the dark ice surface, which allowed a reduced surface albedo that led to an early (mid-April) as well as an extensive, summertime surface melt. The highest concentration of positive anomalies in air temperature, number of melting days and melt extent were observed in the northeast. Tedesco and Fettweis (2020) explained these anomalies with a higher northeastern cloud cover in combination with the low albedo. The first major melt event happened between June 11 and 17 when half of the ice sheet was at melting point (Tedesco and Fettweis, 2020).

The second major melt event took place between July 29 and August 2 with a maximum melt extent of 62%–73% of the GrIS, including the 79 N, on July 30 and 31 (Cullather *et al.*, 2020; Tedesco and Fettweis, 2020). Extensive melt was caused by a northward blocking pattern, which had emerged as a high-pressure ridge over Western Europe and transitioned into a closed-circulation anticyclone over Scandinavia. The blocking pattern led to a bending of the jet stream from the southeast to the northwest, advecting warm air from Europe to Greenland. After arriving at the ice sheet, the warmer air was rapidly mixed down from the mid-troposphere to the ground, initiating strong GrIS melting on July 29 (Tedesco and Fettweis, 2020). Figure 1 depicts the anomalous high 500-hPa geopotential height over northeast Greenland during that time.

Over the 79 N Glacier, the circulation anomaly was associated with an increase of surface pressure and wind speed, a change in wind direction from north/northwest to southerly-to-southwest and a reduction in cloud cover according to ERA5 as a result of the northeastern blocking location, consistent with descriptions in Ward *et al.* (2020). The change in atmospheric conditions led to a rise in air temperatures, which peaked at 7°C near 79 N on July 31. Strongest warming concentrated along the coast. It is likely that the warming effect was reinforced by the southwesterly air masses heating adiabatically as they descended from the interior of the GrIS towards the eastern shoreline (Ward *et al.*, 2020). The rise in surface temperature determined the onset of surface melt. The 79 N (highlighted with the black dot in Figure 2) was located approximately in the transition area of freezing and melting temperatures.

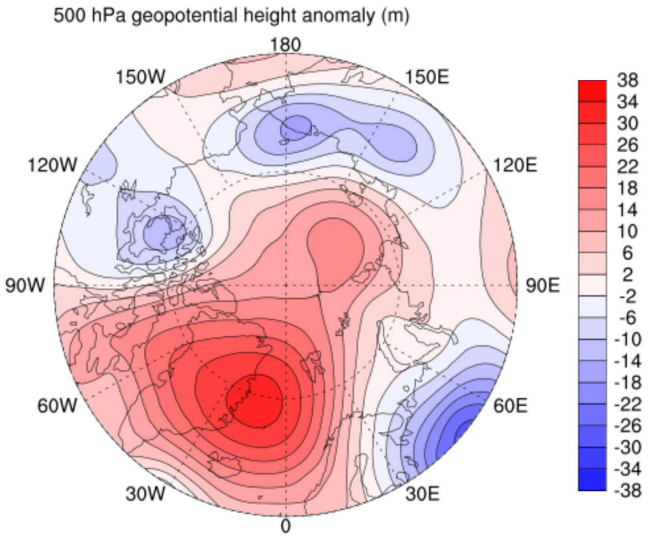

FIGURE 1 ERA5 geopotential height anomalies during peak melting from July 29 to August 1, 2019 relative to the 30-year average 1980–2009 over the days of the study period (July 23 to August 10) [Colour figure can be viewed at wileyonlinelibrary.com]

In its ablation area, temperatures were at the melting point during the period July 30 to August 2, allowing for surface melt and runoff. On subsequent days, the blocking anticyclone weakened and the jet stream shifted back into lower latitudes. As a consequence, surface temperatures dropped below freezing again. During the last days of the study period (August 7–10), an anticyclone established over northeast Canada, leading to a northwesterly inflow of moist air onto northern Greenland. This triggered low but not extreme temperatures and an increase in cloud cover.

2.2 | Polar weather research and forecasting model and setup

The PWRF, a regional atmospheric model adjusted for the Arctic and Antarctica and introduced by Hines and Bromwich (2008), was developed by the Polar Meteorology Group of the Byrd Polar and Climate Research Center at The Ohio State University. Most of the changes relative to the regular Weather Research & Forecasting Model (WRF) (Skamarock *et al.*, 2019) have been made to the physical schemes, mainly the Noah land surface module (LSM), to better represent sea ice and snowpack and their role in heat transfer processes (Hines *et al.*, 2011; Hines *et al.*, 2015). PWRF has undergone extensive testing over the GrIS (Hines and Bromwich, 2008), the Arctic Ocean (Bromwich *et al.*, 2009) and the Arctic land (Hines *et al.*, 2011; Wilson *et al.*, 2011, 2012). Previously it has successfully been used for studies over the NEGIS (Turton *et al.*, 2020; Turton *et al.*, 2021). We used PWRF version 4.1.1, which was the latest at the time of our study.

The model setup was informed by extensive experience from our previous WRF applications and additional polar studies using PWRF (Hines *et al.*, 2011; Barton and Veron, 2012; Turton *et al.*, 2019; Cho *et al.*, 2020; Turton *et al.*, 2020). The best-performing configuration (Table 1) was chosen out of a set of 44 sensitivity runs, testing various combinations of physics, dynamics and time step options. The domain is based on a Polar Stereographic projection centered on northeastern Greenland (Figure 3a). Applying one-way nesting, the horizontal resolution of 5 km in the outer domain (d01) was dynamically downscaled to 1 km in the inner domain (d02). The higher temporal (hourly) and spatial resolution output of the inner domain was used for the present analysis. The high spatial resolution of the nest is necessary due to the complex topography within the domain and to resolve small-scale processes and features of clouds. Thus, the grid spacing is similar to that in previous polar cloud modeling studies with WRF of, for example, Sotiropoulou *et al.* (2021), but

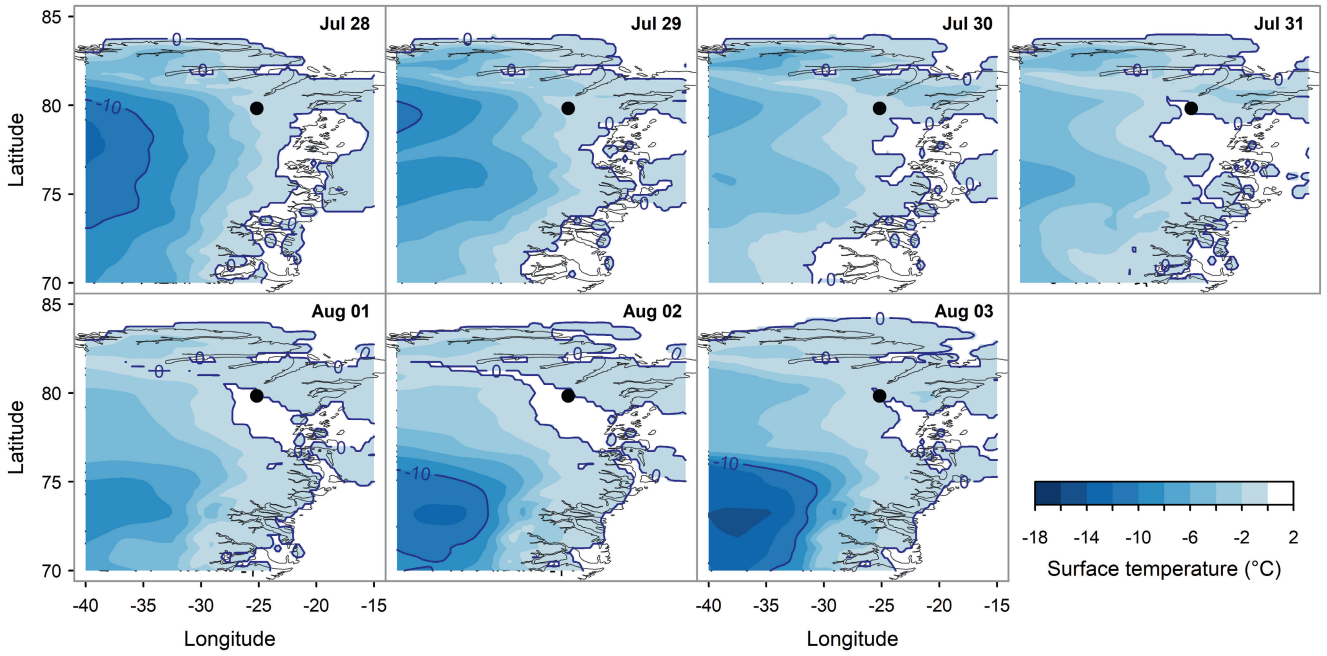

FIGURE 2 ERA5 surface temperature (in °C) over Northeast Greenland during July 28 to August 3, 2019. The blue contour lines show the 0°C and the −10°C lines. The black dot marks the location of KPC_U [Colour figure can be viewed at wileyonlinelibrary.com]

higher than in other publications (e.g., Otkin and Greenwald, 2008; Hines and Bromwich, 2017; Listowski and Lachlan-Cope, 2017; Cho *et al.*, 2020; Sedlar *et al.*, 2020). The model was run for 22 days, covering the period July 21 to August 10, 2019. The first 48 hr were discarded for model spin-up in accordance with previous WRF model studies (e.g., Listowski and Lachlan-Cope, 2017; Kropač *et al.*, 2021).

To comply with the polar setup of WRF, either thresholds or external data on several sea ice variables are specified. Based on analyses of satellite data of the respective days in 2019, sea ice thickness, sea ice albedo and maximum snow depth on sea ice were adjusted to 0.2, 0.64 and 0.3 m, respectively, to better match the conditions at the coast of 79 N.

2.3 | Model input data

The operational European Centre for Medium-Range Weather Forecast (ECMWF) reanalysis dataset ERA5 at hourly intervals served to specify lateral and boundary conditions of the PWRF simulations. Its horizontal resolution is approximately 31 km and it covers 137 vertical levels from the surface until a height of 0.01 hPa. Previous studies employed ERA5 for analyses in the Arctic and over Greenland (e.g., Graham *et al.*, 2019). In addition, Graham *et al.* (2019) found it to perform best in a group of five reanalysis products over the Arctic gateway.

However, snow water equivalent and snow depth values of 2,000 kg·m^{-2} and 10 m, respectively, were indicated by ERA5 almost all over northeast Greenland in August. These exceed typical snow heights measured in summer (Pedersen et al. 2016; Rasmussen et al., 2018). Similar overestimations have been found previously (Wang *et al.*, 2021). To account for the overestimation, the upper bounds of snow water equivalent and physical snow depth, which are both used to determine snow depth, were limited to 300 kg·m^{-2} and 1.0 m respectively in the WRF initial conditions. These values are based on observations of the area and glaciers in the vicinity and have previously been used successfully in studies of the 79 N (e.g., Turton *et al.*, 2020).

To represent sea ice concentration and sea surface temperature (SST) the Optimum Interpolation 1/4 Degree Daily Sea Surface Temperature Analysis developed by the National Oceanic and Atmospheric Administration (NOAA) National Centers for Environmental Information (NCEI) was used (Reynolds *et al.*, 2007; Banzon *et al.*, 2016). The product is based on Advanced Very High Resolution Radiometer (AVHRR) infrared satellite SST data supplemented by *in-situ* data from buoys and ships. Daily data are provided on a 0.25° spatial grid.

2.4 | Evaluation data

Three observational datasets were used to validate the PWRF simulations. In-situ observations at two automatic

TABLE 1 Summary of the most relevant polar-optimized Weather Research & Forecasting Model (PWRF) settings used for the simulations concerning domain configuration, physics and dynamics options and forcing data

Parameter	Selection	References
Domain configuration		
Horizontal grid spacing	5 km (d01) and 1 km (d02)	
Grid dimensions	320 × 320 (d01) and 381 × 381 (d02)	
Time step	30 s (d01) and 10 s (d02)	
Vertical levels	60; lowest eta-level: ∼9.6 m above the surface	
Model top pressure	1,000 Pa	
Physics		
Microphysics	Morrison 2-moments (Morrison *et al.*, 2009)	Barton and Veron (2012), Cho *et al.* (2020), Listowski and Lachlan-Cope (2017), Turton *et al.* (2020)
Cumulus	Kain–Fritsch (only in d01) (Kain, 2004)	Hines and Bromwich (2008), Turton *et al.* (2020)
Radiation	Community Atmosphere Model scheme (Collins *et al.*, 2004)	Barton and Veron (2012), DuVivier and Cassano (2016)
Planetary boundary layer	Mellor-Yamada-Janjić TKE scheme (Janjić, 2002)	Barton and Veron (2012), Cho *et al.* (2020), Turton *et al.* (2019)
Atmospheric surface layer	Eta similarity scheme (Janjić, 1994)	Cho *et al.* (2020), Listowski and Lachlan-Cope (2017), Turton *et al.* (2020)
Land surface model	Unified Noah Land-Surface Model (Chen and Dudhia, 2001)	Barton and Veron (2012), Cho *et al.* (2020), Listowski and Lachlan-Cope (2017), Turton *et al.* (2020), Vignon *et al.* (2019), Wilson *et al.* (2011)
Dynamics		
Diffusion	Calculated in physical space	Kropač *et al.* (2021)
Input data		
Static data	United States Geological Survey (USGS) 24-category land use and land mask	
Lateral boundaries	ERA5 and National Oceanic and Atmospheric Administration (NOAA) Optimum Interpolation 1/4 Degree Daily Sea Surface Temperature Analysis	

weather stations (AWSs) located on Kronprins Christian Land (KPC) in the northeast of Greenland are available from the PROMICE (Programme for Monitoring of the Greenland Ice Sheet) network operated by the Greenland and Denmark Geological Survey (GEUS). As displayed in Figure 3b, the upper station, KPC_U, is located close to the equilibrium line at 79.83°N, 25.17°W, 870 m a.s.l. and the lower station, KPC_L, is located close to the ice sheet margin at 79.91°N, 24.08°W, 370 m a.s.l. (Fausto *et al.*, 2021). Station variables used for the analysis include air pressure, air temperature, specific humidity, wind speed and direction, short- and long-wave radiation, turbulent heat fluxes and surface temperature. The data have been post-processed, including for example a tilt-correction. Refer to Fausto *et al.* (2021) for more information on the PROMICE dataset. We calculated daily surface albedo as the ratio of aggregated hourly up- and downwelling short-wave radiation. Hourly albedo values were capped at a maximum value of 0.9, since values above were considered unrealistic and typically result from measurement uncertainty (Mölg *et al.*, 2009).

Simulated cloud cover fractions were validated with satellite imagery acquired by the multispectral instrument on the Sentinel-2A satellite and the Moderate Resolution Imaging Spectroradiometer (MODIS) Terra. Compared to other datasets such as CloudSat, they offer the advantage of having high spatial and temporal resolutions, providing the potential for a robust cloud detection at high latitudes. Sentinel-2A, previously successfully used for supraglacial lake detection over the 79 N (Hochreuther

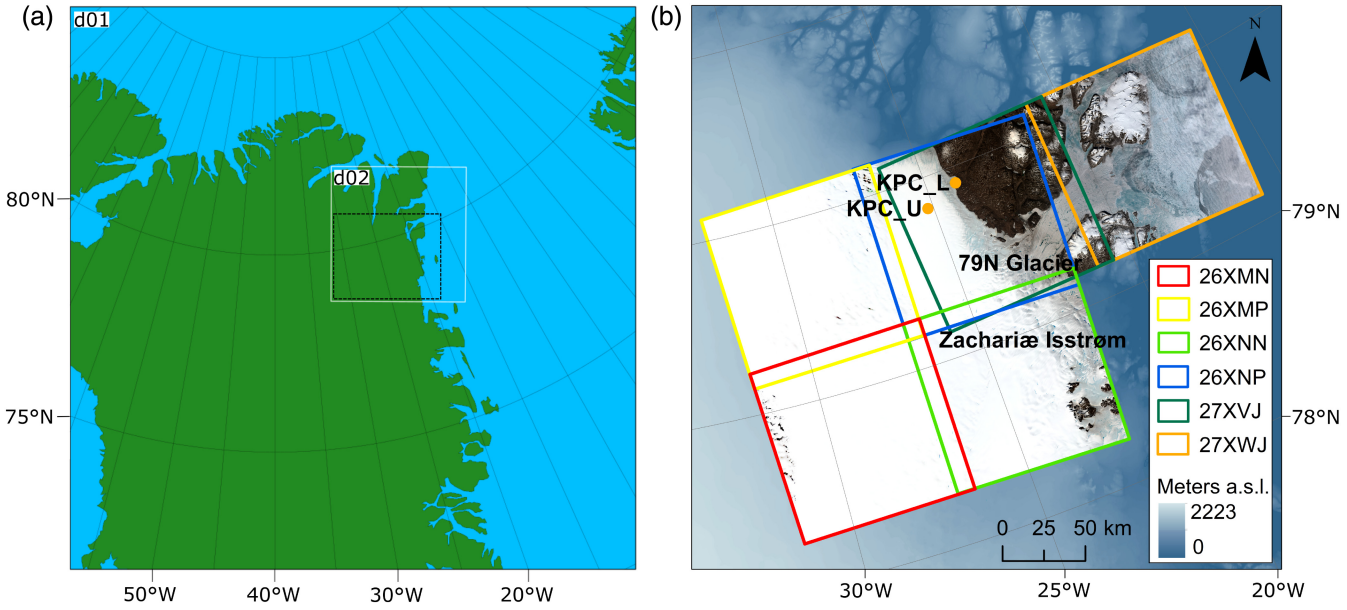

FIGURE 3 Location of the study area. (a) The outer (d01) and inner domain (d02) used for the simulation as well as the validation area (black rectangle). (b) Location of the Sentinel-2A granules and the two PROMICE (Programme for Monitoring of the Greenland Ice Sheet) stations as well as the 79 N and the Zachariæ Isstrøm. The true-color (band combination 4–3-2) image mosaic is of June 19, 2019. The elevation model in the background was produced by the Greenland ice sheet mapping project (Howat *et al.*, 2014) [Colour figure can be viewed at wileyonlinelibrary.com]

et al., 2021), collects images at a horizontal resolution of 10 m with a revisit time of less than two days for the polar regions (European Space Agency, 2015). Level-1C (L1C) scenes of six granules (110 × 110 km, Figure 3b), containing the 79 N, were used. Images were merged separately, delivering one complete scene with a sensing interval of maximum 50 min per day. Each scene was compared to the PWRF output of the closest time. To derive a cloud mask, the widely used algorithm Fmask (Function of mask) (e.g., Tarrio *et al.*, 2020; Hochreuther *et al.*, 2021) was applied to the images as it unites the benefits of a straightforward state-of-the-art application with reasonable results. It creates a 20-m-resolution cloud mask by separating the image into clouds, cloud shadow, clear sky, water and snow (Zhu and Woodcock, 2012). For this study, version 0.5.5 was used.

A cloud mask at 250 m is distributed with the MOD35 product, whereas information on cloud water path (CWP) is provided in the MOD06 product at 1 km spatial resolution (Platnick *et al.*, 2018). In contrast to the Sentinel-2A data, multiple scenes per day were available for the study site. To make them comparable to PWRF simulations at full hour, only those images with a time difference of maximum 15 min and with less than 5% of missing data were retained. All of them were cropped to the extent of the Sentinel-2A granules (Figure 3b).

2.5 | Evaluation procedure

Simulations were evaluated against the PROMICE and satellite observations, using the two grid points closest to the AWS coordinates and spatial averages, respectively. To assess the model performance three different statistical metrics were calculated, including mean model bias (MMB), Pearson Correlation Coefficient (r) and root mean square error (RMSE) (Wilks, 2011).

Liquid water path (LWP) is the vertically integrated sum of all liquid hydrometeors (suspended liquid cloud droplets and falling rain), whereas ice water path (IWP) is the vertically integrated sum of all solid hydrometeors (suspended ice and falling snow and graupel). Within each grid column, the mixing ratios were summed and vertically integrated with respect to the thickness of the vertical layers. Total CWP is the vertically integrated total cloud mixing ratio and includes both, LWP and IWP. Vertically resolved 2D cloud fraction, defined as the area of a grid box covered by a cloud, was column-integrated. To obtain a binary cloud cover mask to compare with the satellite data, a threshold of 10^{-6} kg·kg^{-1} was applied to the total cloud mixing ratio. This value has previously been applied to delineate summer clouds in Antarctica (Hines *et al.*, 2019).

2.6 | Analysis of the cloud effect

As in many previous studies (e.g., Intrieri, 2002; Cox *et al.*, 2015; Wang *et al.*, 2018; Niwano *et al.*, 2019; Wang *et al.*, 2019; Izeboud *et al.*, 2020; Djoumna *et al.*, 2021), we used the cloud radiative effect (CRE) as a metric to assess the impact of clouds on the surface energy balance. It is defined as the difference in $W{\cdot}m^{-2}$ between cloudy and clear-sky surface radiative fluxes under the assumption of unchanged meteorological conditions. A positive CRE implies a net cloud warming at the surface, whereas a negative CRE refers to a net cloud cooling. CRE was calculated using Equation 1 for the short-wave, Equation 2 for the long-wave and Equation 3 for the net effect, where SW↓ and LW↓ are the downwelling short- and long-wave radiation and α is the surface albedo. Like in previous studies (Shupe and Intrieri, 2004; Barton and Veron, 2012), the upwelling component of the long-wave spectrum was ignored in the calculation as it is assumed to be the same during clouded and clear-sky conditions. Following this definition of CRE, the instantaneous cloud effect is considered.

$$\mathrm{CRE}_{\text{short-wave}} = \left(\mathrm{SW}\downarrow_{\text{all-sky}} - \mathrm{SW}\downarrow_{\text{clear-sky}}\right) \times (1-\alpha)\left[W\cdot m^{-2}\right] \quad (1)$$

$$\mathrm{CRE}_{\text{long-wave}} = \mathrm{LW}\downarrow_{\text{all-sky}} - \mathrm{LW}\downarrow_{\text{clear-sky}}\left[W\cdot m^{-2}\right] \quad (2)$$

$$\mathrm{CRE}_{\text{net}} = \mathrm{CRE}_{\text{short-wave}} + \mathrm{CRE}_{\text{long-wave}}\left[W\cdot m^{-2}\right] \quad (3)$$

To further evaluate the relationship between clouds and surface warming or melting, the total surface energy balance (E_{tot}) was calculated using Equation 4, where SHF and LHF are the turbulent sensible and latent heat fluxes, respectively.

$$E_{\text{tot}} = \mathrm{SW}\downarrow\times(1-\alpha) + \mathrm{LW}\downarrow + \mathrm{LW}\uparrow + \mathrm{SHF} + \mathrm{LHF}\left[W\cdot m^{-2}\right] \quad (4)$$

Energy available for melting (E_{melt}, in $W{\cdot}m^{-2}$) equals E_{tot} when surface temperature is at the melting point (0°C). Fluxes are positive when directed toward the surface, indicating a supply in energy, and negative when leaving the surface, corresponding to a loss of energy.

3 | RESULTS & DISCUSSION

3.1 | Model evaluation

Figure 4 compares the model simulations with the PROMICE observations. Since the two KPC stations are located closely to each other and the model performance is similar, we decided to focus on only one station. The upper station, KPC_U, was chosen as it combines the advantages of better representing the conditions over the 79 N as well as the interior, which experienced exceptional surface melt, and is far enough from the ice sheet margin, where the barren surroundings could bias the data.

Overall, the near-surface properties at 79 N are realistically reflected by PWRF. Surface air pressure and wind speed are all-round well captured (not shown), having a correlation coefficient of $r = 0.97$ and $r = 0.71$, respectively. While the temporal variability of air temperature (Figure 4a), SW↓ (Figure 4c) and LW↓ (Figure 4d) is moderately to well captured, their absolute values are not always well represented. Parts of the differences can most likely be attributed to the difference in measurement height. However, it should be noted that radiative fluxes are simulated with higher skill at KPC_L (SW↓: MMB = $-8.55\,W{\cdot}m^{-2}$, $r = 0.90$, RMSE = $65.29\,W{\cdot}m^{-2}$; LW↓: MMB = $1.80\,W{\cdot}m^{-2}$, $r = 0.47$, RMSE = $27.73\,W{\cdot}m^{-2}$). Variability in specific humidity (Figure 4e), wind direction (Figure 4f) and surface albedo (Figure 4b) are only moderately captured. The daily surface albedo values agree well at the beginning of the simulation. Then, however, the model values decrease logarithmically as the snow ages, while the observed values remain almost constant. During each modeled snow fall event, which is the case twice at the end of the study period (August 9 and 10), the albedo value instantly leaps back to its maximum value. Since these snow fall events are not visible in the observations, this leads to an only moderate correlation coefficient at KPC_U. At KPC_L, albedo is overestimated.

While PWRF has amendments to the Noah LSM, these are mostly to better represent sea ice (Hines *et al.*, 2015), whereas glacier albedo is still poorly represented. In order to solve the deviations in albedo, several tests were performed, including changes in the physical parametrization and the input meteorological fields. In Noah LSM, surface albedo is directly related to snow cover. Every time fresh snow falls, the albedo jumps to its maximum value and decays afterwards as a function of the age of the snow (Livneh *et al.*, 2010; Hines *et al.*, 2011). As long as the ground is still snow-covered, the albedo does not drop below the minimum value set in the model code. Thus, an accurate representation of snow cover is indispensable to realistically simulate surface albedo. During the study period, ERA5 snow depth had an almost constant value of 10 m over the entire land area except for a narrow coastal strip where it dropped sharply down to zero. Although being lowered before ingesting them into the model (Section 2.3), values remained too high, never dropping below 0.2 m except for an isolated area at the coast. Thus, snow extent was constant and darker glacier ice or

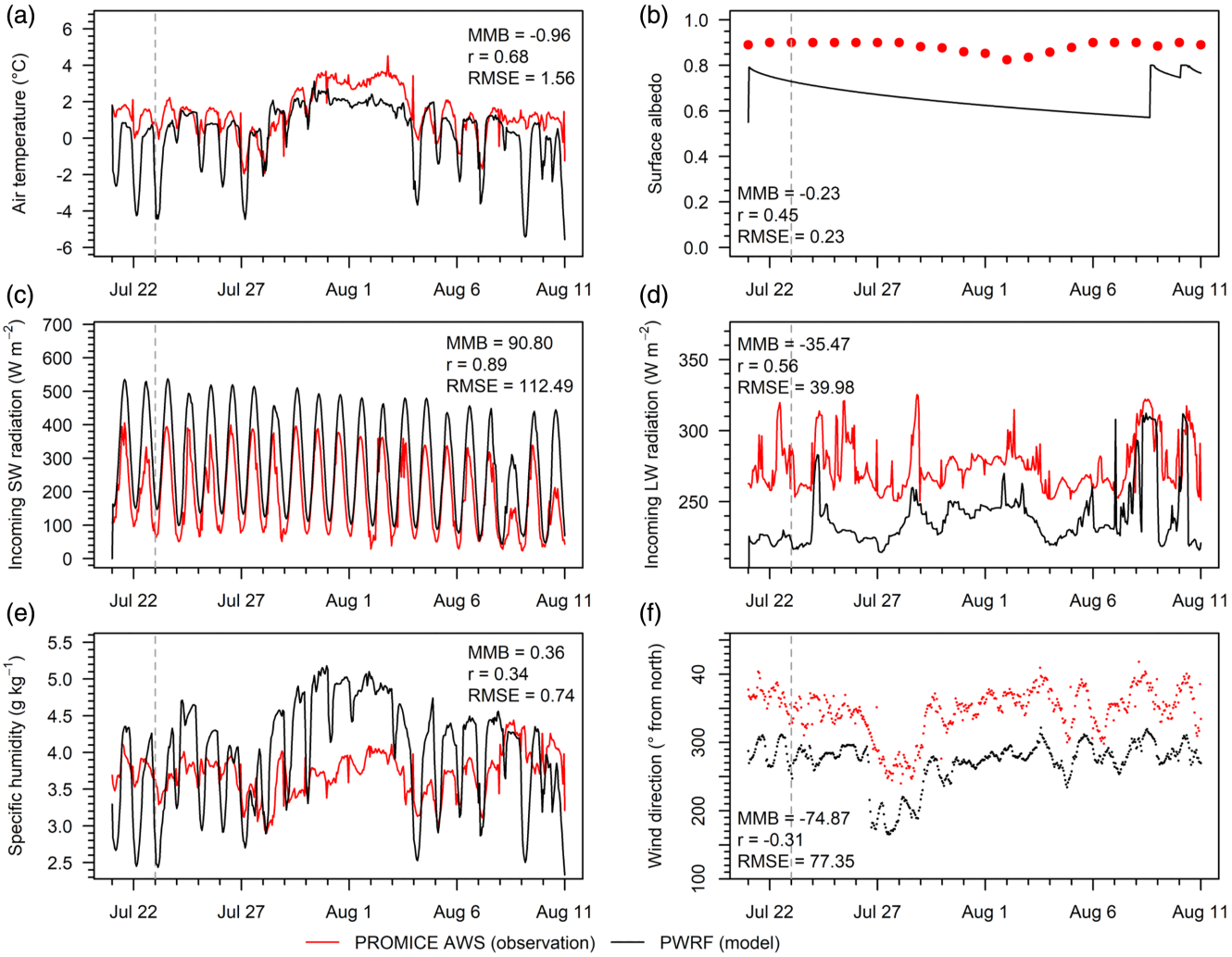

FIGURE 4 Comparison of modeled (black line) meteorological surface variables of the respective closest grid cell with ground measurements (red line) at KPC_U. The gray dotted line separates the spin-up period. Note that at times with calm wind the wind direction equals zero. AWS, automatic weather station; MMB, mean model bias; PWRF, polar-optimized Weather Research & Forecasting Model; RMSE, root mean square error [Colour figure can be viewed at wileyonlinelibrary.com]

the bare ground at the coast was not represented. Considerable snow depth overestimation by ERA5 was also detected for High Mountain Asia (Wang *et al.*, 2021), the Yamal Peninsula in Russia (Matveeva and Sidorchuk, 2020) and for the Tibetan Plateau (Orsolini *et al.*, 2019).

Despite the deficiency in modeled surface albedo, the statistical performance metrics are predominantly in the range of previous model evaluations of hourly WRF simulations (e.g., Hines and Bromwich, 2008; Bromwich *et al.*, 2009; Collier *et al.*, 2018; Temme *et al.*, 2020; Turton *et al.*, 2020; Kropač *et al.*, 2021), suggesting sufficient model skill to use the model output in the further analyses of the cloud effect.

Accurate information about the spatial distribution of clouds and their macro- and microphysical properties is required to understand cloud radiative forcing on the underling surface. PWRF captures the absolute values as well as the temporal variability in cloud cover (Figure 5a) and CWP (Figure 5b) reasonably well, reflecting the observed three stages of cloud cover (Figure 5a): medium cloud coverage at the beginning, low cloud cover during peak melt and high cloud cover at the end. A more detailed analysis, however, reveals certain mismatches. Occasionally (e.g., July 24 and 28), PWRF simulates the arrival of cloud fields earlier than in the observations, leading to large overestimations. At other instances, however, the possible time difference between the simulation at full hour and the acquisition of the satellite images (MODIS $\pm$ 15 min, Sentinel-2A $\pm$ 50 min) must be considered (Section 2.4). Especially during times of atmospheric instability, such as during the last days, cloud cover is variable and states alternate quickly.

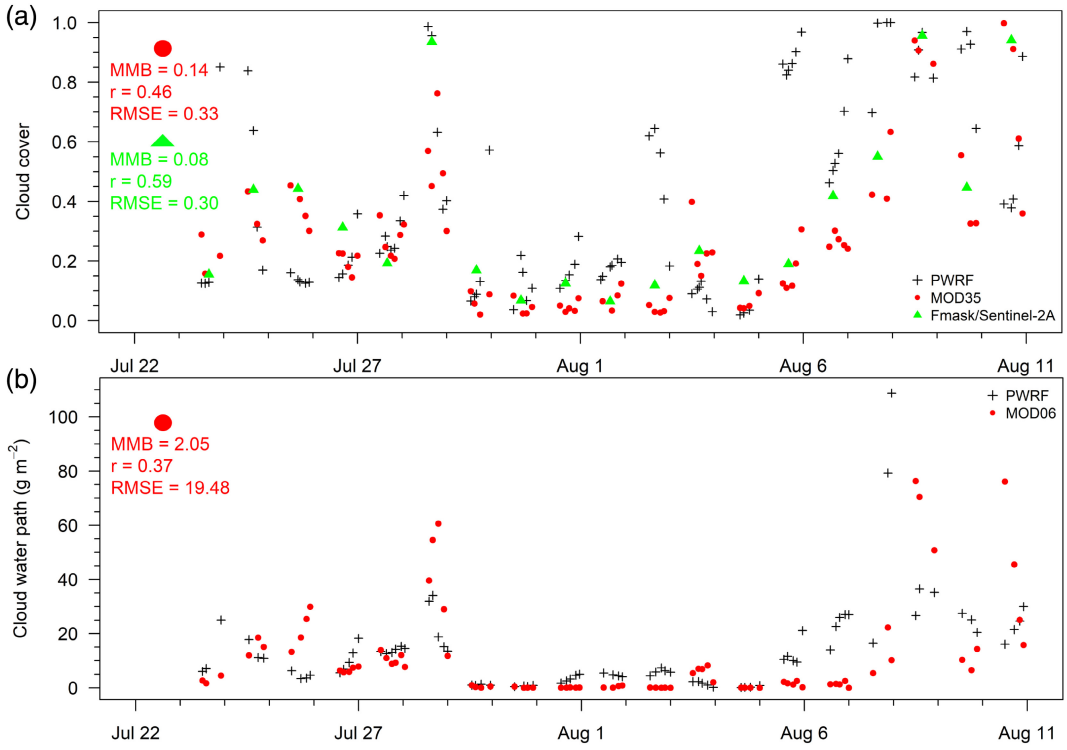

FIGURE 5 Spatial averages of cloud properties in the PWRF model simulations and satellite datasets observed by MODIS and Sentinel-2A. (a) Cloud cover as the ratio of the validation domain being clouded. Black crosses represent the total simulated cloud cover, while red dots show the MOD35 and green triangles the Fmask/Sentinel-2A results. (b) Total cloud water path (CWP, liquid and ice particles) in the model simulation (black crosses) and MOD06 (red dots). Note that only the PWRF time steps are displayed that can be compared to either MODIS or Sentinel-2A data. Fmask, function of mask; MMB, mean model bias; PWRF, polar-optimized Weather Research & Forecasting Model; RMSE, root mean square error [Colour figure can be viewed at wileyonlinelibrary.com]

Spatiotemporally averaged, cloud cover is highest (41.1%) in the simulations, followed by the results of Fmask (36.3%), and lowest in the MOD35 product (26.8%). Some differences in the results may be due to the different methods to determine cloud cover in the simulation and satellite data (Section 2.5). The apparent model overestimation is mostly caused by the sensitivity of the applied total cloud water mixing ratio (Section 2.5) to detect very thin clouds at high altitudes and the tendency of PWRF to simulate many of these. Even though high-level clouds are less important for cloud radiative forcing than their lower counterparts (Bennartz *et al.*, 2013; Miller *et al.*, 2017), they are common over Greenland (Lenaerts *et al.*, 2020). In remotely sensed data, clouds over bright surfaces are difficult to detect due to the limited spectral contrast. Optically thin clouds (e.g., cirrus) are a particular challenge because of their shared spectral signature with the underlying earth′s surface (Zhu and Woodcock, 2012). As for the Fmask algorithm, the absence of a thermal band in the Sentinel-2A imagery impedes the detection of low-altitude clouds, since the cirrus band can only partially account for the missing information (Frantz *et al.*, 2018). Consequently, it frequently fails at detecting low- and mid-altitude clouds (Frantz *et al.*, 2018; Chen *et al.*, 2020), while actually being good for the detection of high-level cirrus clouds (Zhu *et al.*, 2015). Visual inspection of the Sentinel-2A images, however, revealed that some optically thin clouds were not detected. Figure 6 shows, using the example of July 25, that although the majority of the clouds are captured, some thin ones are missed in the southeast. As thin cirrus clouds with small reflectance values are difficult to discern by visual inspection, it is possible that the number of undetected thin clouds is even higher in the other images, similarly reported in other studies (e.g., Zhu and Helmer, 2018; Tarrio *et al.*, 2020).

MODIS also frequently misses thin clouds. Thresholds used for the detection of clouds need to be sufficiently high in order to avoid noises in its cirrus band 26 that could be confused with thin clouds, the so-called electronic "crosstalk" problem (Guenther *et al.*, 2002). While being good for optically thick clouds, MODIS thus has an inferior capability to detect optically thin clouds (Holz *et al.*, 2008; King *et al.*, 2013)—a problem that persists even in the latest MODIS collections (Tan *et al.*, 2019; Kotarba, 2020; Lee *et al.*, 2020). Tan *et al.* (2019) found the

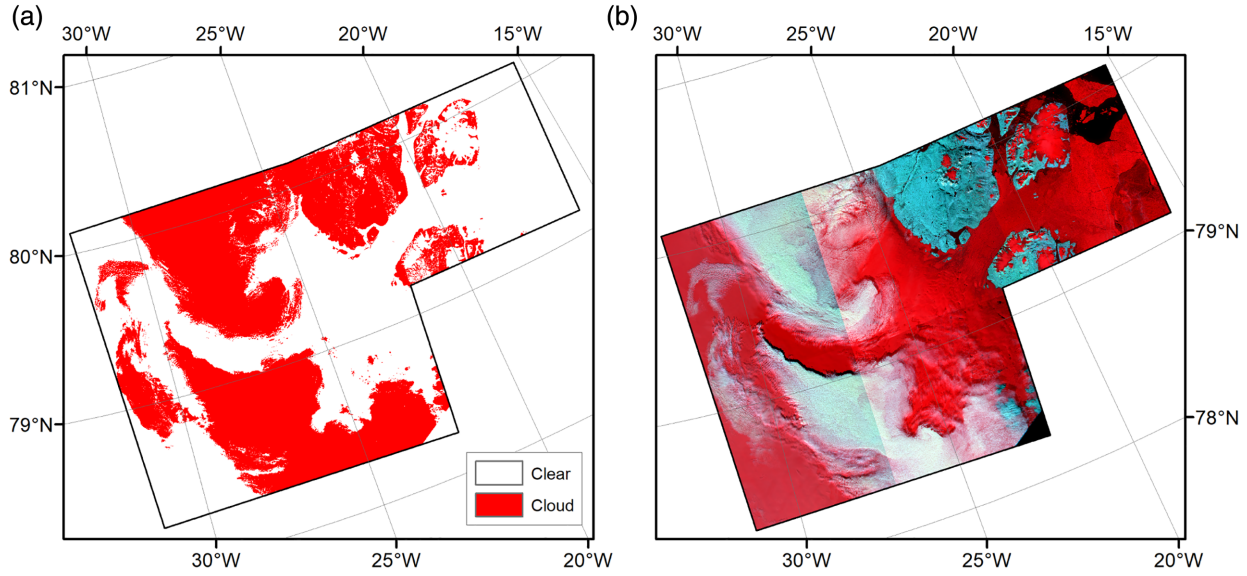

FIGURE 6 (a) Cloud mask obtained by the Fmask algorithm and (b) a false-color composite (band combination 2–11-12) of Sentinel-2A for July 25, 2019. In the false-color composite, clouds appear white, whereas thick ice and snow surfaces stand out in vivid red, barren ground as well as rocks are colored bright cyan and deep water is black. Fmask, function of mask [Colour figure can be viewed at wileyonlinelibrary.com]

strongest discrepancy between CALIOP (Cloud-Aerosol Lidar with Orthogonal Polarization) and MODIS Collection 6 data at low cloud optical thickness (COT) values, which has been confirmed for Collection 6.1 used in this study (Kotarba, 2020). While PWRF allows for very thin clouds with water contents frequently below 0.01 $g \cdot m^{-3}$ and COT values below 0.4, the MODIS cloud mask detects clouds only reasonably well until a COT of 0.4 and thinner clouds are commonly omitted by the passive sensor (Ackerman *et al.*, 2008; Tan *et al.*, 2019). Uncertainties are found to be highest in the polar regions, where cloud amount is underestimated by up to 40%, particularly at night when only thermal bands are available (Kotarba, 2020). Further, Chan and Comiso (2013) found that in the Arctic, low- (top height <2 km) and high-level clouds (top height >6 km), especially when they are geometrically thin (<2 km), are an important source of error, as they are frequently missed by MODIS. For example, on July 24 and 28, PWRF simulates an almost completely overcast sky in the afternoon (Figure 5a). Fmask results for July 28 also show overcast conditions, while cloud cover is below 50% in MODIS on both days. This is because PWRF simulates many thin ice clouds (Figure 8d). While the higher-level ice clouds over the darker 79 N and adjacent land are detected by MODIS, the sensor missed those further inland over the brighter ice sheet. In contrast, Fmask detected most ice clouds in the interior, while it failed to capture the low clouds over the 79 N on July 24. Considering the described shortcomings and the generally better capabilities of the sensor over open water than over snow and ice surfaces (Liu *et al.*, 2010), it is assumed that not all clouds over the ice sheet and the sea ice were observed. The underestimation of the cloud amount also affects the results of related cloud properties, as these are only calculated for pixels flagged as cloudy or probably cloudy in the cloud mask.

Applied to Sentinel-2 images, Fmask commonly misclassifies bright surfaces (i.e., bare soils, snow and ice) as clouds (Frantz *et al.*, 2018; Chen *et al.*, 2020). To account for the separation problem between clouds and artificial surfaces, the algorithm was improved (Frantz *et al.*, 2018), yet this has not solved the problem over snow-covered areas (Chen *et al.*, 2020; Hochreuther *et al.*, 2021; Zekoll *et al.*, 2021). In many scenes, the rocky outcrops in the eastern part of study area are mistaken for clouds (Figure 6), causing an overestimation of total cloud cover. The misidentification of high-elevation sites as clouds is a frequent problem in the Fmask results (Qiu *et al.*, 2019; Cilli *et al.*, 2020).

The model and satellite data disagree most often in the coastal area, particularly over the tongue of the 79 N, where an almost permanent cloud cover is simulated (Figure 7b). Disagreement in this area is particularly high with Fmask data, which show clear conditions over the glacier tongue in more than 50% of the scenes. The deficiency in the detection of thin clouds may also account for the discrepancy between the satellite products and the model simulations of the fog and low-level cloud cover over the tongue of the 79 N. Summertime fog is a frequent feature over the Arctic Ocean (Tjernström *et al.*, 2012) and over east Greenland (Gilson *et al.*, 2018) as well as

over the 79 N Glacier (personal communication Ole Zeising, December 6, 2021). Previous studies with MODIS images showed that fog extent over the low-lying part of the outlet glacier was highest at the end of July and the beginning of August (Jiskoot *et al.*, 2019). Generally, the existence of thick sea ice limits or even prevents the formation of Arctic sea fog and low-level stratus as the vertical moisture flux is reduced and the boundary layer is more stable (Paluch *et al.*, 1997). For the simulation period, the default sea ice thickness was reduced, based on observed values (Section 2.2). The thin and patchy sea ice allows for an increase in atmospheric moisture from the Arctic Ocean and the formation of marine stratus. Simulated optical thickness in the lowest levels was predominantly low (COT < 3), complicating the detection by remote sensors.

Mismatch in many instances is likely to be a consequence of the shortcomings of the satellite products in the polar regions. Previous studies have proven the good performance of the Morrison 2-moment microphysics in the polar regions (e.g., Listowski and Lachlan-Cope, 2017; Cho *et al.*, 2020). Therefore, model simulations are assumed to be sufficiently accurate to further analyze the cloud radiative impact.

3.2 | Cloud properties

The following analysis focuses on the landmasses in the inner domain (d02 in Figure 3a) using exclusively model output. The ocean area was masked out in all spatial averages due to the strong contrast of cloud cover over land and sea, and due to our focus on the impact of clouds on surface melting. It further increases the comparability with preceding studies.

We classified clouds into low- (top height < 2 km), mid- (2 km < top height < 6 km) and high-level clouds (top height > 6 km), a classification that has previously been applied (Chan and Comiso, 2013). In the lowest level, shallow clouds account for 21% of the area on average (Figure 7a). Compared to low-level clouds, high-level clouds have higher geometrical depths and the highest spatial coverage of 16% at around 7.8 km. Mid-level clouds only play a subordinate role at most times with a maximum mean occurrence of 14% at the transition to the high-level. The bimodal distribution is similar to previous PWRF results for the Arctic (Cho *et al.*, 2020). Nevertheless, mid-level clouds could be underrepresented, likely as a result of insufficient vertical mixing in the Mellor-Yamada-Janjić planetary boundary scheme (Otkin and Greenwald, 2008). Over the whole study period and area, mean total cloud cover (as vertical integral) is 45% (Figure 7b), which is lower than the GrIS-wide summer mean of 66% (2007–2010) (van Tricht *et al.*, 2016), but roughly agrees with previous annual-mean model results for the region (Ettema *et al.*, 2010) and reflects the blocking conditions. Generally, the lower cloud fractions in the northeast are likely to be a consequence of the drier atmosphere and the dominant wind system. However, cloud occurrence follows a clear gradient from the interior to the coast, where summertime fog and low-level marine stratus are an almost permanent feature due to the regular supply of moisture. Cloud occurrence decreases toward the interior as the temperature and moisture decrease. It is subject to a higher temporal variability due to the diminishing influence of the ocean and the increasing importance of the atmospheric circulation and regional wind patterns, resulting in stronger temporal contrasts. However, the comparison with the AWS observations in Section 3.1 indicated that simulated total cloud cover in the upper ablation zone is either underestimated or optically too thin, visible in the higher simulated than observed SW↓ and lower LW↓.

Figure 7c shows the vertical distribution of cloud cover over the case study period. Only toward the end of the study period, when the impact of the anticyclone subsides, longer lasting high cloud covers are simulated. Also, cloud cover increases at all levels, reaching fractions of above 0.9. Another extensive high-level cloud shield is simulated prior to the melt event on July 28. However, it passes by within a few hours, allowing for high incident solar radiation thereafter. Very few clouds are simulated during the time of the strongest surface melting.

Over most of the study period, LWP, which is almost completely represented by cloud droplets (Figure 8b), quantitatively dominates IWP with a mean value of 12.3 $g \cdot m^{-2}$ compared to 8.3 $g \cdot m^{-2}$ (Figure 8a). However, the IWP maximum is more than twice as high (160.0 $g \cdot m^{-2}$) as the LWP maximum (66.4 $g \cdot m^{-2}$). These highlights are caused by short-term sharp increases of ice and snow water content or suspended cloud liquid water. In contrast to these three major hydrometeor categories (also found in Cho *et al.*, 2020), graupel and rain only contribute little to total CWP. When only considering grid points flagged as cloudy, mean LWP is 27.2 $g \cdot m^{-2}$. Forty-two percent of these grid points have a LWP above 10 $g \cdot m^{-2}$ and 19% are in the range of 10 and 40 $g \cdot m^{-2}$, which was previously shown to elicit the highest radiative effect (Bennartz *et al.*, 2013). Clouds within this range are opaque enough to reflect the long-wave surface emission while being thin enough to allow for SW↓ to be absorbed by the surface and to raise near-surface temperature. The high percentage of clouds with a LWP below 10 $g \cdot m^{-2}$ further corroborates the finding that PWRF simulated many thin clouds and vast thick cloud covers were mostly absent during the study period.

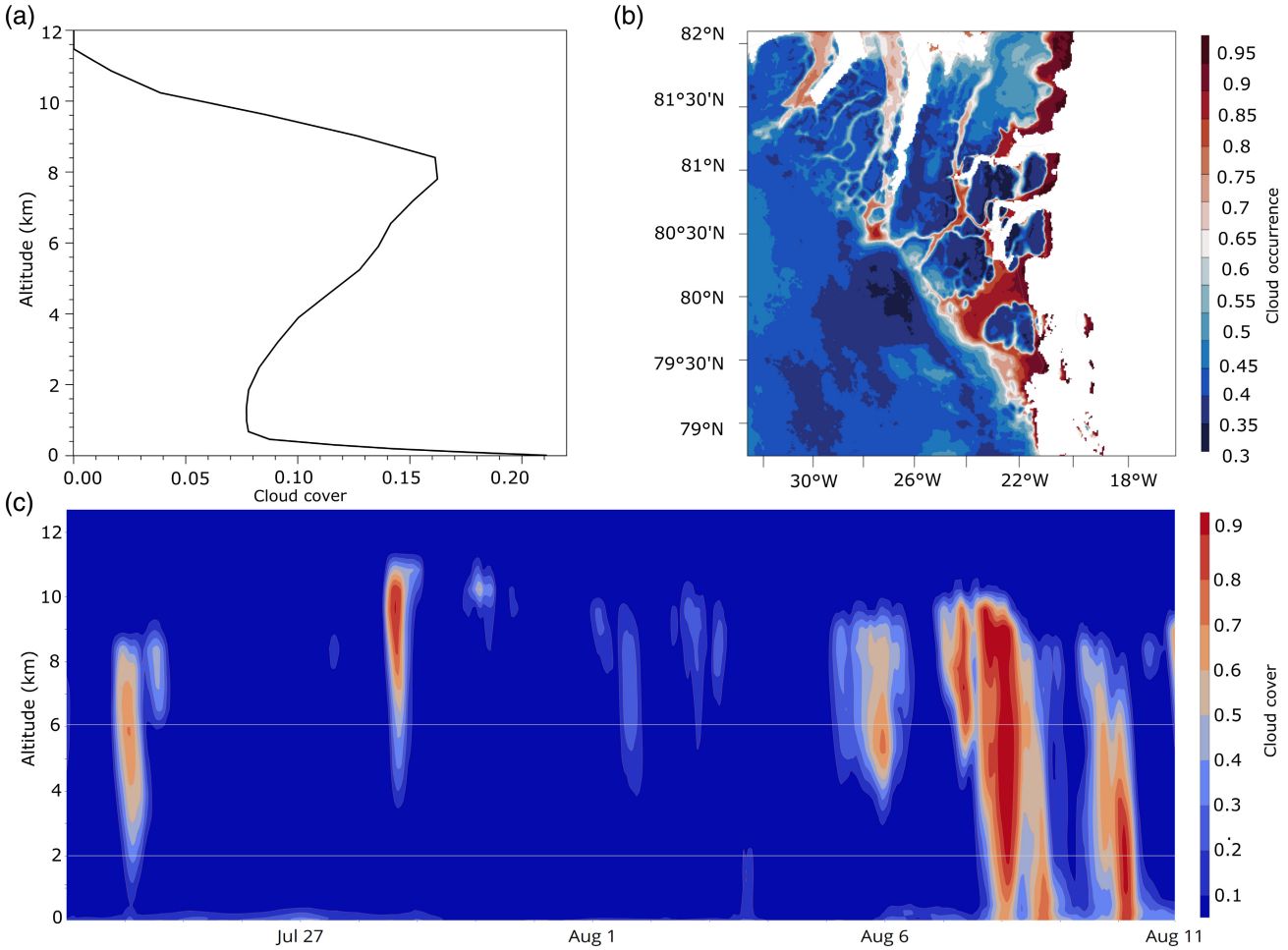

FIGURE 7 Temporal and spatial cloud cover distribution over land. (a) Vertical mean distribution of simulated mean cloud cover per vertical level using the total cloud water mixing ratio threshold. (b) Mean total cloud occurrence. The color scheme represents the frequency of cloud cover per grid point during the study period. Note that the ocean area was masked out in the calculations. (c) Temporal and vertical distribution of simulated cloud cover. Horizontal lines discriminate between low- (<2 km), mid- (2–6 km) and high-level clouds (>6 km) [Colour figure can be viewed at wileyonlinelibrary.com]

The anticyclonic conditions during the study period are also reflected in the lower mean LWP and IWP compared to results for most of Greenland (van Tricht *et al.*, 2016; Lenaerts *et al.*, 2020), which, however, did not cover the northern-most part. When excluding the period of the strongest melting (July 29 to August 4), during which CWP was extremely low, the mean value of LWP (16.4 $g \cdot m^{-2}$) aligns with the average of 16.0 $g \cdot m^{-2}$ found in observations for JJA by van Tricht *et al.* (2016). Simulated IWP is slightly lower (12.4 $g \cdot m^{-2}$) than their Greenland-wide mean (19.0 $g \cdot m^{-2}$), but a strong decreasing trend in their cloud cover is visible toward the north, indicating below-average values over the NEGIS (van Tricht *et al.*, 2016; Lacour *et al.*, 2017). Moreover, their Greenland-wide mean value is strongly distorted by the extraordinary high IWP in the southeast.

The most important contribution to CWP comes from low-level clouds. In contrast to cloud cover, which is also high in the upper troposphere at many time steps (Figure 7c), Figure 8e shows that total cloud water content peaks almost exclusively near the surface (~0.08 $g \cdot m^{-3}$). At higher altitudes, simulated cloud water contents are predominantly low (<0.05 $g \cdot m^{-3}$), indicative of frequent clear conditions or the presence of thin ice clouds. The reason for the strong contrast is the different quantitative contributions of the hydrometeors. Suspended cloud liquid water is more abundant in proximity to the Arctic Ocean, which acts as permanent moisture source. Therefore, the highest contents appear close to the ground with a spatiotemporal mean value of 0.03 $g \cdot m^{-3}$ and isolated peaks up to 0.08 $g \cdot m^{-3}$ (Figure 8b). Whereas cloud liquid water predominates below 1 km most of the time, its vertical extent increases toward the mid-level with changing synoptic conditions. Any supercooled liquid present in the upper layers is readily converted into ice at low temperatures. Therefore, icy hydrometeors concentrate in

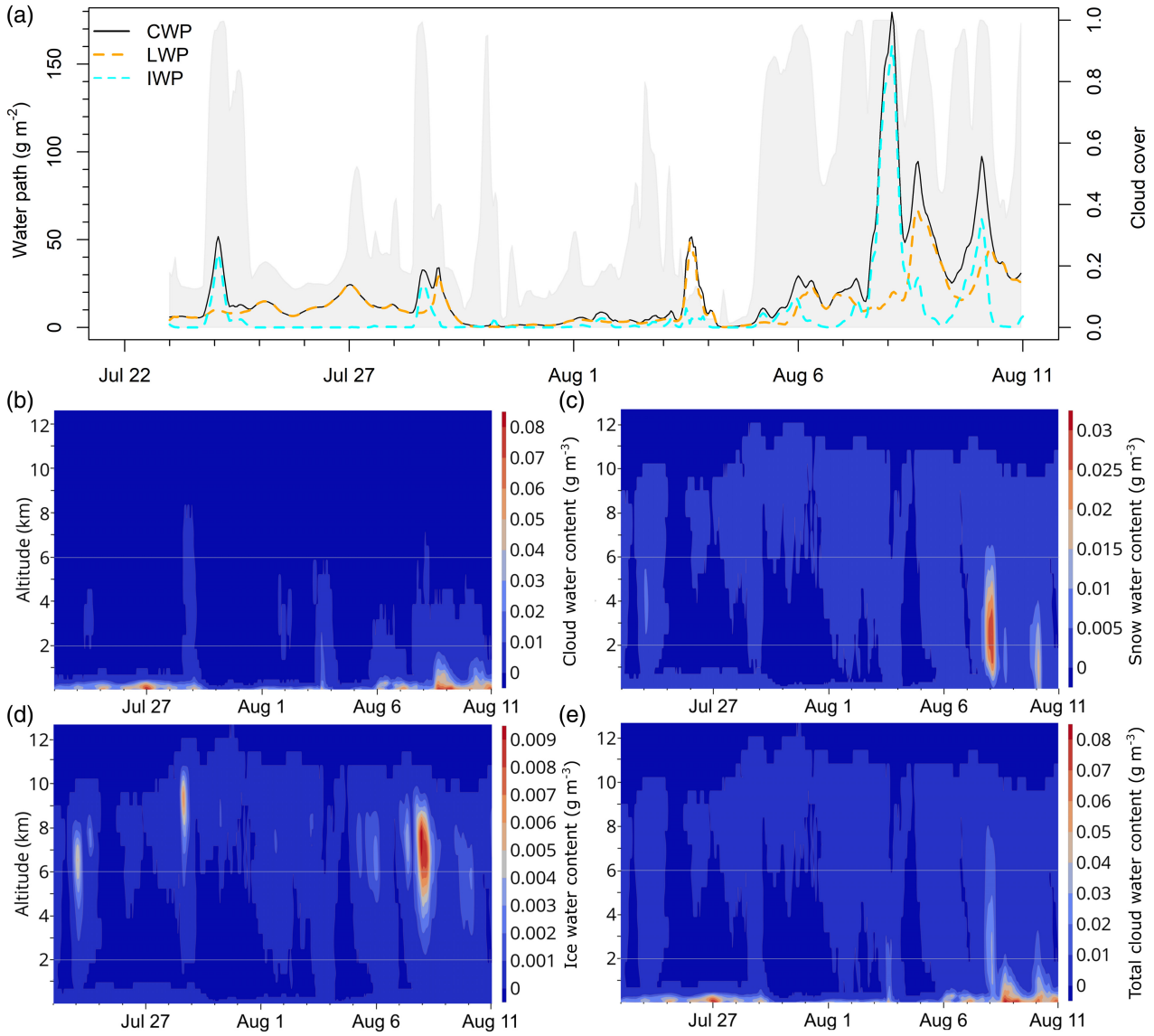

FIGURE 8 Temporal and spatial distribution of simulated cloud water over land. (a) Spatially averaged total (CWP), liquid (LWP) and ice water path (IWP). Shaded area displays the temporal evolution of area-averaged cloud cover. Vertical distribution of (b) cloud, (c) snow, (d) ice, (e) total water content (also including rain and graupel) as mean of each vertical model layer. Horizontal lines discriminate between low- (<2 km), mid- (2–6 km) and high-level clouds (>6 km) [Colour figure can be viewed at wileyonlinelibrary.com]

the middle and high layers (> ~4 km). While ice water contents are above zero at most times steps, record values of almost 0.01 $g \cdot m^{-3}$ are visible from August 7 to 8 (Figure 8d). Snow peaks at slightly warmer conditions at around 1.9 km and also has its maximum of 0.03 $g \cdot m^{-3}$ from August 7 to 8 (Figure 8c). The amounts of simulated graupel and rain are negligible.

3.3 | Cloud radiative effect

Spatially averaged long-wave (short-wave) CRE ranges from 0.7 to 62.9 $W \cdot m^{-2}$ (−34.6 to −0.3 $W \cdot m^{-2}$) with a mean value of 18.2 $W \cdot m^{-2}$ (−6.9 $W \cdot m^{-2}$) (Figure 9a). Net CRE is dominated by its positive long-wave component, resulting in overall warming effects. Clouds add around 11.2 $W \cdot m^{-2}$ to the radiation received at the surface. There are only few exceptions where the net effect is negative. CRE exhibits a similar temporal variability as the cloud properties (Figure 8a). The highest cloud effects are achieved during times of high cloud amount and water, while CRE approaches zero at times of the strongest melting.

Cloud cover is a first-order control on CRE and determines its spatial distribution (Figure 9c–e): long-wave (short-wave) CRE sharply rises (decreases) in proximity to the Arctic Ocean due to the increasing cloud

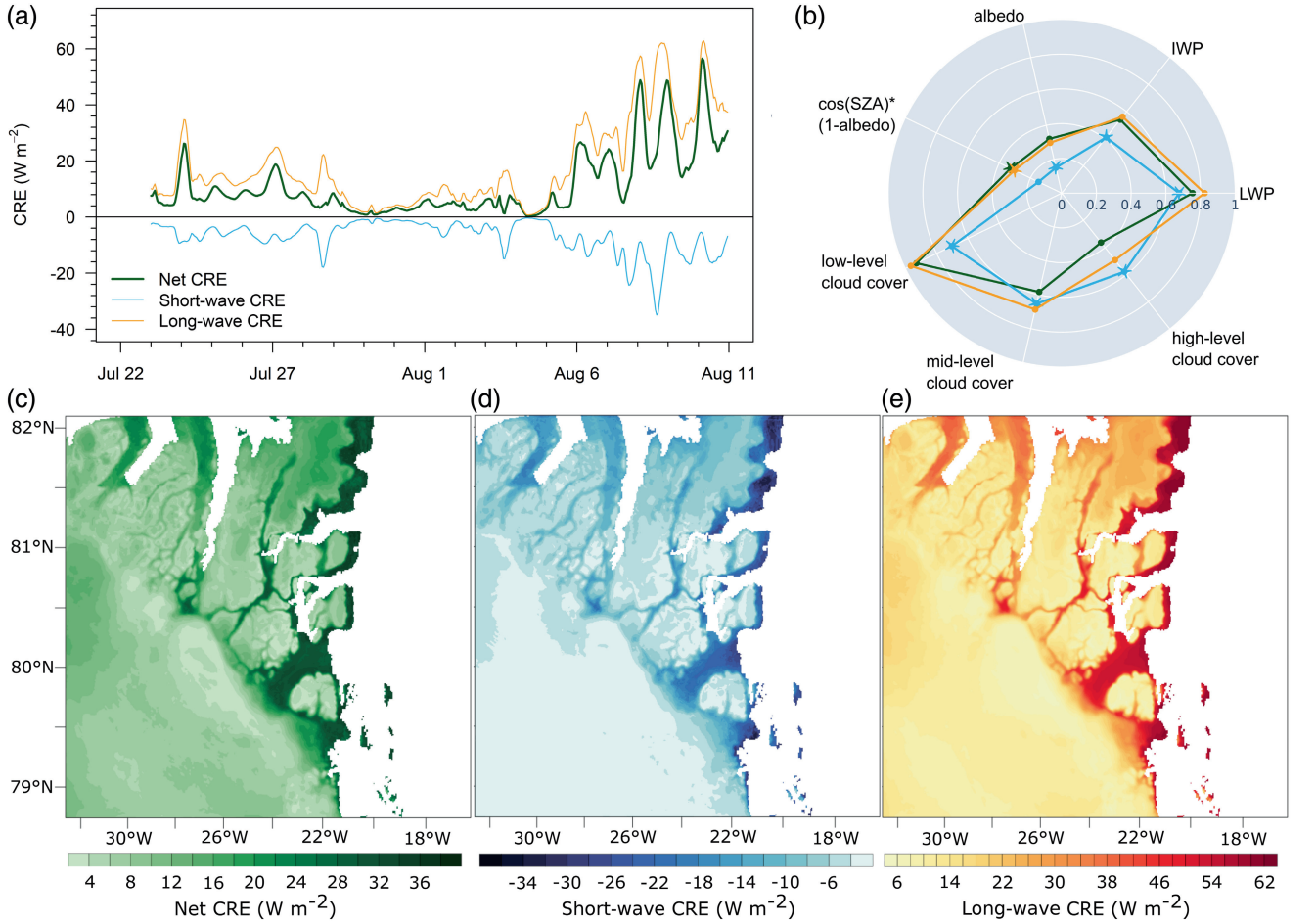

FIGURE 9 Cloud radiative effect (CRE) during the study period over land. (a) Spatial averages of CRE, (b) Pearson correlation coefficients with net CRE (black), short-wave CRE (blue), long-wave CRE (orange) and cloud properties (LWP, liquid water path; IWP, ice water path), where negative correlations are marked with an asterisk, and temporal mean of (c) net CRE, (d) short-wave CRE and (e) long-wave CRE. All shown correlation coefficients are statistically significant at $p < 0.01$. Cos(SZA)*(1 − albedo) is the cosine of the sun solar zenith angle (SZA) multiplied with one minus the surface albedo and is often used to assess the cloud radiative impact. For more explanations refer to the text in Section 3.3 [Colour figure can be viewed at wileyonlinelibrary.com]

amount, corroborating the findings by Wang *et al.* (2019). In contrast, differences are minor further inland and insignificant between the ablation and the accumulation zone probably due to the overall high surface albedo, which leads to a reflection of most of the incoming radiation.

However, the strength of the correlation (Figure 9b) with cloud cover decreases with cloud altitude. Low- and mid-level cloud cover both correlate highly with long-wave ($r_{low} = 0.96$ and $r_{mid} = 0.69$) and net CRE ($r_{low} = 0.93$ and $r_{mid} = 0.58$), while short-wave CRE is less strongly and negatively correlated ($r_{low} = -0.70$ and $r_{mid} = -0.65$), suggesting that the shading not solely depends on the simple coverage. Correlations with high-level clouds are only moderate and subject to a higher variability. The weaker correlations are presumably a consequence of the lower COT and cloud temperature at high altitudes. Therefore, long-wave warming and short-wave shading are stronger for optically opaque clouds. The higher correlation (by |0.2|) with LWP than IWP suggests that the effect is more important for liquid- than for ice-bearing clouds. Differences are the result of the diverging effective radii and shapes related to the thermodynamic phase of the hydrometeors: The typically smaller but numerous droplets in liquid clouds have a greater surface area per volume, increasing the opacity and the albedo (Curry, 1995; Shupe and Intrieri, 2004). Since the opacity is directly related to the radiative transmissivity, clouds with higher water concentrations shade more solar irradiance (Zhang *et al.*, 1996; Sedlar *et al.*, 2020). Similarly, their emissivity in the infrared spectrum increases, but saturates when reaching the characteristics of a blackbody (Shupe and Intrieri, 2004). From that moment on, LW↓ is determined predominantly by cloud temperature (Bennartz *et al.*, 2013).

This explains the range of LWP (10 and 40 g·m^{-2}) of which the cloud radiative forcing is most sensitive (Shupe and Intrieri, 2004; Bennartz *et al.*, 2013).

Surface albedo, as well as the combined effect with SZA, only weakly correlate with CRE (r_{LW} = |0.30|, r_{SW} = |0.15|, r_{net} = |0.32|). Correlations are slightly stronger when only considering the cloudy states (r_{SW} = 0.46, r_{net} = 0.55), since during clear states the absence of cloud water limits the feedback with albedo and SZA. This effect has already previously been shown by Minnett (1999) and Wang *et al.* (2018). The latter suggested that at high sun elevations (large cos(*SZA*)) over low-albedo areas, clouds scatter more of the solar radiation, causing a stronger short-wave CRE. As suggested by Wang *et al.* (2018), this can explain, why short-wave CRE, in contrast to the long-wave component, does not saturate at high LWP. Instead an increase in LWP leads to a further strengthening of the short-wave CRE, making net CRE at high LWP primarily dependent on the SZA and albedo (Wang *et al.*, 2018). Given the average high surface albedo values and the limited sun elevations at the study site at the end of July and beginning of August, this helps to understand the constant dominance of long-wave warming and the low correlations with the combined SZA and albedo effect.

3.4 | Surface melt contribution

On the first days of the study period, only coastal areas experience melting during the day, while the remaining parts of the research domain have simulated surface temperatures below the melting point. A strong decrease in the amount of E_{melt} is simulated on July 27, marking the transition to the anticyclonic conditions (Figure 10). With the impinging anticyclone, the wind speed and air temperature rise, which leads to an increase in the amount and the extent of E_{melt} on the following days. By July 29, the entire northeast sector is melting. The supply of melt energy increases over the next few days, peaks on August 2 with a domain average of 104.2 W·m^{-2}, which is approximately twice as high as in the beginning, and decreases thereafter (Figure 10). While E_{melt} is still high at the coast on August 3, the spatially averaged melt potential continuously decreases on subsequent days due to lower values and a smaller affected area. At the end of the study period, only some coastal areas are still at the melting point. Averaged over time and space, 26.6 W·m^{-2} is available for melting. While mean values are highest (40–50 W·m^{-2}) in the north and along a narrow strip in the lower ablation area, E_{melt} averages 20–30 W·m^{-2} over the 79 N.

Unsurprisingly, net short-wave radiation dominates the diurnal cycle of E_{melt}. Also in the long-term, the increase of net short-wave radiation during cloud-free times and decrease at the end of the study period due to the increase in SZA and cloud shading correlates moderately with E_{melt} (r = 0.41, p < 0.1). In contrast, net long-wave radiation shows no clear correlation with melt. Its increase to −38.2 W·m^{-2} during the last days compared to the mean of −57.1 W·m^{-2} is related to the higher cloud cover. On a daily basis, the amount of E_{melt} correlates only weakly with net CRE (r = −0.35) and long-wave CRE (r = −0.32). The correlation coefficient is even lower for short-wave CRE (r = 0.26). Hence, surface melt tends to be higher during times of low cloud coverage. However, the connection is not statistically significant at p < 0.01. This underlines the competing effects of long- and short-wave cloud surface forcing. Moreover, highlighting that determinants other than clouds that are at play.

Contributions of the turbulent fluxes are much smaller and more variable. During the strongest melting (July 28 to August 3), surface cooling through sublimation and evaporation (LHF = −20.4 W·m^{-2}) is compensated by the positive SHF. While occasionally removing energy from the surface before the extensive melt (July 24 to 27), the latter gains in importance as wind speeds increase and the temperature gradient between the warm atmosphere and the cooler surface of the ice sheet rises and is a decisive factor in the widespread surface warming and melting in northeast Greenland. During peak melt, SHF is on average 29.0 W·m^{-2}, contributing 28.2% to the energy balance (Figure 10). Contributions are especially high during daily minimum SW↓, providing a maximum of 42.2 W·m^{-2} or 52.4%. This suggests that cooling of the surface at night was limited. Positive contributions of SHF are sustained also outside the extreme melting period. This is related to a more rapid cooling of the snow and ice surface through long-wave infrared emission than of the overlying air. It is assumed that the gradient is even enhanced due to condensation processes in the almost permanent fog layer over the low-elevation areas, visible in the slightly positive LHF during the times of daily minimum SW↓.

We hypothesize that the blocking anticyclone in the northeast is accompanied by foehn winds, remotely triggered by an antecedent atmospheric river event in the northwest, an effect only recently highlighted (Mattingly *et al.*, 2020; Mattingly *et al.*, 2022). These dry and warm downslope winds cause positive SHF and net short-wave radiation anomalies as well as negative LHF and net long-wave radiation anomalies, increasing E_{melt}. On July 26, an atmospheric river developed on the west coast of Greenland evident in MERRA-2 (Modern-Era Retrospective analysis for Research and Applications, Version 2) data used in Mattingly *et al.* (2022). By the end of July 28, the atmospheric river moves eastwards across Greenland, though losing water vapor amount. On July 29, a sudden

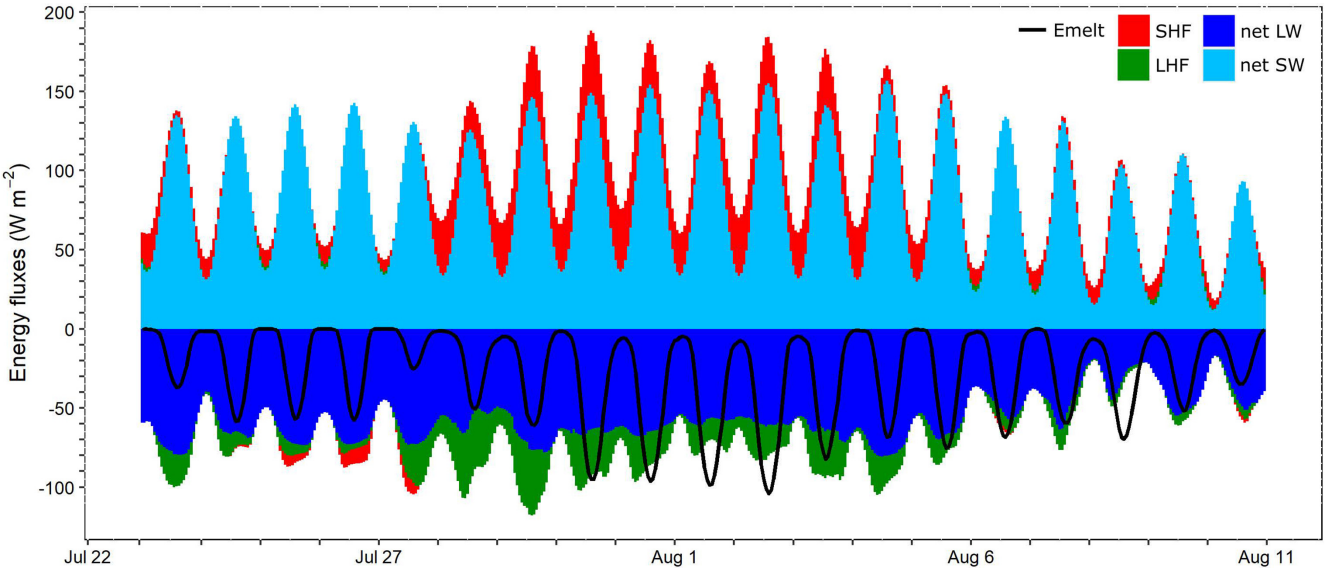

FIGURE 10 Hourly surface energy balance and energy available for melting (E_{melt}) averaged over the study area. E_{melt} is equal to the net energy balance at the ground (E_{tot}) when the surface temperature is at the melting point. E_{melt} of all grid cells with lower surface temperatures was set to zero for the calculation of the spatial averages. Incoming fluxes are positive and relate to a warming, whereas outgoing fluxes are negative and correspond to a cooling. Since E_{melt} removes energy from the surface, it must be displayed as a negative flux. LHF, latent heat flux; net LW, net long-wave radiation; net SW, net short-wave radiation; SHF, sensible heat flux [Colour figure can be viewed at wileyonlinelibrary.com]

drop in relative humidity, a change in wind direction, together with a jump in wind speed and a sharp increase in air temperature was simulated at KPC_U (Figure 4a,f). Similar characteristics reoccur on August 1 and 2. These conditions are characteristic of foehn winds, although they are not well documented in this region. Therefore, we hypothesize that a weak foehn wind, prompted by an atmospheric river, enhances the melting. Besides the enhancement of SHF, the incipient foehn winds also dispel most of the fog and low-level marine stratus over the low-lying coastal area, including the floating tongue of the 79 N, allowing for more incident solar radiation. This effect is strongest on July 29, when the entire glacier tongue is fog-free. On subsequent days, the fog-dissolving effect is less evident even under reoccurrence of the foehn winds, suggesting that the anticyclone slowly moves on and the drying impact of the foehn winds is not strong enough.

Hence, our results suggest that the combined impact of high net short-wave radiation and SHF drove the extensive surface melt on the NEGIS. Without the contribution of this turbulent flux, surface melting would have been less strong and extensive. Non-radiative fluxes were previously highlighted by Fausto *et al.* (2016b) as dominant drivers of the exceptional melt event in 2012. Hofer *et al.* (2017) linked the decrease in summer cloud cover in 1995–2009, in response to more anticyclonic conditions, with enhanced melting. However, they identified the decreased cloud shading in the ablation zone as cause. Contradictory to Hofer *et al.* (2017), this analysis reveals that clouds had a permanent long-wave warming effect over the NEGIS during the study period. Although the absence of clouds increased SW↓, the exceptional amount and extent of the melting would not have occurred without the direct warming and drying impact of the anticyclone-induced warm-air advection and the foehn winds. Clouds were more important after the anticyclone had abated. Despite the subsequent cooler and less windy conditions and reduced SW↓, owing to the increasing SZA and higher cloud cover, the long-wave warming effect from the clouds sustained surface melting. The clouds between August 5 and 10 added on average 22.9 W·m^{-2} to the surface energy balance every hour. Although E_{melt} was 33% lower than at the highest melt between July 29 and 4, melt energy was 72% higher compared to July 23 to 28, when only few clouds were present and net CRE was 50% lower.

3.5 | Impact of surface albedo

A positive CRE of a similar range had previously been observed at KPC_L and KPC_U during May to August 2008–2013 by Wang *et al.* (2019). On the other hand, compared to the observations (Section 3.1), simulated surface albedo is found to be overestimated in the lower

ablation area and slightly underestimated in the upper ablation zone during our study period. A realistic surface albedo representation, however, is decisive for an accurate calculation of the surface energy balance because (besides SZA) its value directly determines the proportion of incident solar radiation that is absorbed by the surface. Fausto *et al.* (2016a) showed that after surface albedo had decayed from 0.6 to 0.2 at an AWS station in southern Greenland, absorption increases by a factor of 2 to 4.

To determine the impact of the bias in the surface albedo on the calculation of CRE, a test was conducted, using simulated values for all variables except for the albedo, which was taken from the AWS observations. Figure 11 shows the results for KPC_U station. There, the occasionally negative net CRE in the model output disappears, and spatially and temporally averaged net CRE is on average 64% higher than before and the magnitude of short-wave CRE decreases by 69%. In contrast, in areas of overestimated surface albedo, the short-wave effect increases due to less incident solar radiation being reflected at the surface and net CRE frequently becomes negative. The higher (lower) surface reflectivity reduces (increases) both the available melt energy and the number of melt hours.

The tendency toward a dominating summertime short-wave CRE in regions of low surface albedo values as opposed to the positive net CRE in the high albedo zones aligns with previous studies (Miller *et al.*, 2015; Solomon *et al.*, 2017; Wang *et al.*, 2018; Izeboud *et al.*, 2020). Whether a cooling effect occurs, depends strongly on surface albedo. Solomon *et al.* (2017) suggested an approximate albedo threshold of 0.8 as the boundary of a warming and a cooling effect. Results by Wang *et al.* (2018), on the other hand, showed that also areas with a lower albedo (~0.5) can experience positive net CRE values. In the present study setup, the boundary appears to comply with the latter one. This suggests that during the melting season the cloud effect found with the model simulations rather applies to areas with higher surface albedo values such as in the accumulation area or in the higher-elevation ablation zone, while during times of higher albedo in spring and autumn they are also realistic for the lower ablation zone. Importantly, the study highlights the strong sensitivity of the cloud impact on external factors, explaining the strongly variable results found in literature for the northeast GrIS.

4 | CONCLUSIONS

Despite the complex topography in the research area and the highly variable nature of clouds, PWRF is capable of simulating realistic magnitudes of cloud cover, water content and water path. The horizontal and vertical extensions of clouds are well captured, not only in the lower but also in the middle to upper troposphere. Some overestimation relative to MODIS and Sentinel-2A cloud retrievals occurs near the surface along the coast, including the floating tongue of the 79 N. However, the satellite data have considerable weaknesses and therefore cannot be considered free of errors. Without a denser network of *in-situ* measurements, it is difficult to determine whether the higher cloud frequency and water content is due to a model bias, such as excessive moisture or insufficient vertical mixing, or because of inadequacies in the comparative data. Nevertheless, comparison with the satellite data as well as with the literature confirms that the model output is within the expected range. Some deviation from previous studies is due to the short study period, which does not represent the average conditions in summer. Since the main features and transitions in cloud properties are reflected, the results allow for insights into processes, particularly the interplay of radiation, cloud properties and surface melting. In view of the paucity of *in-situ* observations in the remote and hostile northeast of Greenland, PWRF is a valuable tool, which holds the potential to complement our knowledge on cloud properties and their radiative and thermal impact.

In northeast Greenland, clouds have a dominant long-wave warming effect in the high-albedo snow- and ice-covered areas during the study period. They can also cool the surface, after the albedo has decreased enough. This underlines the competing impact clouds have on the near-surface climate conditions in the lower ablation zone and complements previous findings (e.g., Wang *et al.*, 2019; Izeboud *et al.*, 2020). At the time of the extreme surface melting, an extensive cloud cover was mostly absent due to the blocking anticyclone. Consequently, cloud effects were negligible. Instead, melt was driven by a symbiosis of different factors, including warm-air advection, cloud dissipation and foehn winds. These favored above-average SW↓ and SHF and outweighed losses through LW↑ and LHF. It is hypothesized that the effect of the anticyclone was reinforced by foehn winds over the northeastward sloping edges. These further promoted the dissipation of clouds also over the almost permanently cloudy or foggy floating tongue of the 79 N through drying and warming the near-surface air ("foehn clearing"), allowing for more incident solar radiation and amplified turbulent heat fluxes. Although clouds were not the decisive instantaneous factor for the peak melting, they had an important effect shortly before and after the event. Clouds were not only more abundant just prior to maximum melt, but also JJA mean cloud cover anomalies were positive in the northeast (Tedesco and Fettweis, 2020). It is assumed that average

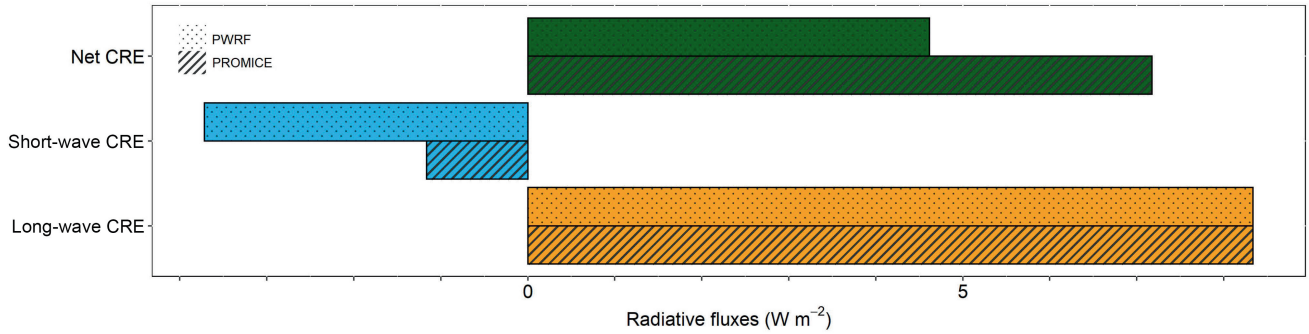

FIGURE 11 Difference in area averaged cloud radiative effect (CRE) when using the observed surface albedo at KPC_U (dotted pattern) compared to CRE with polar-optimized Weather Research & Forecasting Model (PWRF) albedo (hatched pattern). PROMICE, Programme for Monitoring of the Greenland Ice Sheet [Colour figure can be viewed at wileyonlinelibrary.com]

higher cloud cover, although variable, preconditioned the ground and allowed for more melting as its long-wave emission overcompensated the losses in solar radiation. The importance of optically thin clouds, as the ones described by Bennartz *et al.* (2013), that prime the surface and prolong the melt around predominantly SW↓ and SHF-driven melt events has previously also been shown for Antarctica (Gilbert *et al.*, 2020).

Surface albedo is an important modulator and determines the sign of the cloud impact. In comparison with *in-situ* observations in the region, simulated albedo was too high and decayed too slowly in the lower ablation zone, largely dampening the short-wave cooling effect and probably concealing spatial differences between the coast and the interior. If the simulated surface albedo was lower in the coastal area, clouds would have had a stronger solar shading effect. Thus, the simulations are assumed to be most realistic for higher-elevation areas and off-peak melt seasons as the albedo changes over the course of the melting season. An improved surface albedo representation is necessary to evaluate spatiotemporal differences comprehensively.

The results demonstrate the complex role that Arctic clouds play in the near-surface climate conditions and the surface mass balance of the NEGIS. Determining the magnitude and sign of their radiative and thermal impact remains challenging, as the cloud effect does not solely depend on the coverage, but also on cloud properties as well as on environmental characteristics. Yet the study complements previous findings for the whole of Greenland (e.g., Wang *et al.*, 2018; Wang *et al.*, 2019; Izeboud *et al.*, 2020) and enhances the understanding of linkages between the atmosphere and the cryosphere. Further it connects previous findings of the general impact of Arctic clouds (e.g., Bennartz *et al.*, 2013; van Tricht *et al.*, 2016; Wang *et al.*, 2018; Wang *et al.*, 2019; Izeboud *et al.*, 2020) with analyses of the causes of the extreme melting in July/August 2019 (Cullather *et al.*, 2020; Tedesco and Fettweis, 2020), improving the understanding of the processes that drove the exceptional melt in the northeast.

Future work should also investigate the long-term cloud effects and the feedback with other components of the climate system. Moreover, a more realistic representation of surface albedo in PWRF and accurate snow cover input data are needed. This also calls for more reliable validation data. In spite of the efforts that have been undertaken to continuously improve the Fmask algorithm (Frantz *et al.*, 2018) as well as the MOD35 cloud mask (Moeller *et al.*, 2017), cloud detection in polar regions remains an unresolved challenge for passive imaging sensors. The limited accuracy of the satellite observations points out the need for more sophisticated algorithms to extract cloud cover information, for example with machine- or deep-learning algorithms (e.g., Chen *et al.*, 2022; Li *et al.*, 2022). Additionally, more comprehensive *in-situ* observations in this region are necessary to validate the model output with a higher degree of confidence.

The expected increase in moisture content in the warming Arctic (Vihma *et al.*, 2016) and the growing moisture supply from the Arctic Ocean in response to the reducing sea ice (Serreze and Meier, 2019) will most likely enhance the cloud cover frequency over Greenland, especially over low-lying areas such as the termini of the outlet glaciers. On the other hand, more prevalent anticyclonic conditions in previous years have been associated with a cloud cover reduction (Hofer *et al.*, 2017). However, these only favor the dissipation of clouds when they are located over northeast Greenland (Ward *et al.*, 2020). Considering the large sea-level rise equivalent stored in the marine-terminating glaciers of the NEGIS, cloud-enhanced surface melt could have tremendous global implications. It is therefore necessary

to further improve our knowledge on Arctic cloud properties and their impact on surface melt.

AUTHOR CONTRIBUTIONS

Jenny V. Turton: Conceptualization; formal analysis; supervision; writing – review and editing. **Thomas Mölg:** Conceptualization; funding acquisition; methodology; supervision.

ACKNOWLEDGEMENTS

This study was supported by the German Federal Ministry for Education and Research (BMBF) and forms part of the GROCE project (Greenland Ice Sheet/Ocean Interaction) (Grant 03F0778F). We acknowledge the High-Performance Computing Centre (HPC) at the University of Erlangen-Nürnberg's Regional Computation Center (RRZE), for their support and resources while running the case study. We also thank Ole Zeising from the Alfred-Wegener Institute (AWI) for providing additional information on the meteorological conditions over the 79 N. ERA5 data were retrieved from the Copernicus Climate Data Store (https://cds.climate.copernicus.eu/cdsapp\LY1\textbackslash#!/search?type=dataset, last accessed on July 5, 2021). The Optimum Interpolation 1/4 Degree Daily Sea Surface Temperature Analysis was obtained from the Research Data Archive at National Center for Atmospheric Research (NCAR) (https://doi.org/10.5065/EM0T-1D34, last accessed on June 25, 2021). Authors are also grateful for the PROMICE AWS network, whose data were downloaded from https://www.promice.dk (last accessed on June 17, 2021). Thanks also to Philipp Hochreuther for the support in the download of the Sentinel-2A L1C scenes from the Google cloud storage using the Google Cloud SDK repository for Ubuntu (https://cloud.google.com/storage/docs/public-datasets/sentinel-2?hL=de, last accessed on June 29, 2021). The Fmask algorithm used for the processing of the Sentinel-2A data was retrieved from http://www.pythonfmask.org/ (last accessed on May 25, 2021). The MODIS data were downloaded from the open-access data portal Level-1 and Atmosphere Archive & Distribution System (LAADS) Distributed Active Archive Center (DAAC) operated by NASA (https://ladsweb.modaps.eosdis.nasa.gov/search/, last accessed on October 31, 2021). We also thank Ella Gilbert and the second anonymous reviewer for their constructive feedback, which improved and clarified the manuscript. Open Access funding enabled and organized by Projekt DEAL.

CONFLICT OF INTERESTS

The authors declare that they have no conflict of interests.

ORCID

Malena Andernach https://orcid.org/0000-0002-9586-720X

REFERENCES

Ackerman, S.A., Holz, R.E., Frey, R., Eloranta, E.W., Maddux, B.C. and McGill, M. (2008) Cloud detection with MODIS. Part II: validation. *Journal of Atmospheric and Oceanic Technology*, 25(7), 1073–1086.

An, L., Rignot, E., Wood, M., Willis, J.K., Mouginot, J. and Khan, S.A. (2021) Ocean melting of the Zachariae Isstrøm and Nioghalvfjerdsfjorden glaciers, Northeast Greenland. *Proceedings of the National Academy of Sciences of the United States of America*, 118(2), e2015483118.

Andersen, J.K., Fausto, R.F., Hansen, K., Box, J.E., Andersen, S.B., Ahlstrøm, A.P., et al. (2019) Update of annual calving front lines for 47 marine terminating outlet glaciers in Greenland (1999–2018). *GEUS Bulletin*, 43, e2019430202.

Banzon, V., Smith, T.M., Chin, T.M., Liu, C. and Hankins, W. (2016) A long-term record of blended satellite and in situ sea-surface temperature for climate monitoring, modeling and environmental studies. *Earth System Science Data*, 8(1), 165–176.

Barton, N.P. and Veron, D.E. (2012) Response of clouds and surface energy fluxes to changes in sea-ice cover over the Laptev Sea (Arctic Ocean). *Climate Research*, 54(1), 69–84.

Bennartz, R., Shupe, M.D., Turner, D.D., Walden, V.P., Steffen, K., Cox, C.J., Kulie, M.S., Miller, N.B. and Pettersen, C. (2013) July 2012 Greenland melt extent enhanced by low-level liquid clouds. *Nature*, 496(7443), 83–86.

Blau, M.T., Turton, J.V., Sauter, T. and Mölg, T. (2021) Surface mass balance and energy balance of the 79N glacier (Nioghalvfjerdsfjorden, NE Greenland) modeled by linking COSIPY and polar WRF. *Journal of Glaciology*, 67(266), 1–15.

Bromwich, D.H., Hines, K.M. and Bai, L.-S. (2009) Development and testing of polar weather research and forecasting model: 2. Arctic Ocean. *Journal of Geophysical Research*, 114(D8), D08122.

Cesana, G., Kay, J.E., Chepfer, H., English, J.M. and Boer, G. (2012) Ubiquitous low-level liquid-containing Arctic clouds: new observations and climate model constraints from CALIPSO-GOCCP. *Geophysical Research Letters*, 39(20), L20804.

Chan, M.A. and Comiso, J.C. (2013) Arctic cloud characteristics as derived from MODIS, CALIPSO, and CloudSat. *Journal of Climate*, 26(10), 3285–3306.

Chen, F. and Dudhia, J. (2001) Coupling and advanced land surface-hydrology model with the Penn State-NCAR MM5 modeling system. Part I: model implementation and Sensivity. *Monthly Weather Review*, 129(4), 569–585.

Chen, X., Liu, L., Gao, Y., Zhang, X. and Xie, S. (2020) A novel classification extension-based cloud detection method for medium-resolution optical images. *Remote Sensing*, 12(15), 2365.

Chen, Y., Weng, Q., Tang, L., Liu, Q. and Fan, R. (2022) An automatic cloud detection neural network for high-resolution remote sensing imagery with cloud–snow coexistence. *IEEE Geoscience and Remote Sensing Letters*, 19, 1–5.

Cho, H., Jun, S.-Y., Ho, C.-H. and McFarquhar, G. (2020) Simulations of winter Arctic clouds and associated radiation fluxes using different cloud microphysics schemes in the polar WRF: comparisons with CloudSat, CALIPSO, and CERES. *Journal of Geophysical Research-Atmospheres*, 125(2), e2019JD031413.

Cilli, R., Monaco, A., Amoroso, N., Tateo, A., Tangaro, S. and Bellotti, R. (2020) Machine learning for cloud detection of globally distributed Sentinel-2 images. *Remote Sensing*, 12(15), 2355.

Clausen, H.B., Gundestrup, N.S., Johnsen, S.J., Bindschadler, R. and Zwally, J. (1988) Glaciological investigations in the Crête area, Central Greenland: A search for a new deep-drilling site. *Annals of Glaciology*, 10, 10–15.

Collier, E., Mölg, T. and Sauter, T. (2018) Recent atmospheric variability at Kibo summit, Kilimanjaro, and its relation to climate mode activity. *Journal of Climate*, 31(10), 3875–3891.

Collins, W., Rasch, P., Boville, B., McCaa, J., Williamson, D., Kiehl, J., et al. (2004) *Description of the NCAR Community Atmosphere Model (CAM 3.0) (No. NCAR/TN-464+STR)*. Boulder, Colorado: UCAR/NCAR.

Cox, C.J., Walden, V.P., Rowe, P.M. and Shupe, M.D. (2015) Humidity trends imply increased sensitivity to clouds in a warming Arctic. *Nature Communications*, 6, 10117.

Cullather, R.I., Andrews, L.C., Croteau, M.J., DiGirolamo, N.E., Hall, D.K., Lim, Y.-K., et al. (2020) Anomalous circulation in July 2019 resulting in mass loss on the Greenland ice sheet. *Geophysical Research Letters*, 47(17), e2020GL087263.

Curry, J.A. (1995) Interactions among aerosols, clouds, and climate of the Arctic Ocean. *The Science of the Total Environment*, 160–161, 777–791.

Curry, J.A., Rossow, W.B. and Schramm, J.I. (1996) Overview of Arctic cloud and radiation characteristics. *Journal of Climate*, 9(8), 1731–1764.

Djoumna, G., Mernild, S.H. and Holland, D.M. (2021) Meteorological conditions and cloud effects on surface radiation balance near Helheim glacier and Jakobshavn Isbræ (Greenland) using ground-based observations. *Frontiers in Earth Science*, 8, 616105.

DuVivier, A.K. and Cassano, J.J. (2016) Comparison of wintertime mesoscale winds over the ocean around southeastern Greenland in WRF and ERA-interim. *Climate Dynamics*, 46(7–8), 2197–2211.

Ettema, J., van den Broeke, M.R., van Meijgaard, E. and van de Berg, W.J. (2010) Climate of the Greenland ice sheet using a high-resolution climate model—part 2: near-surface climate and energy balance. *The Cryosphere*, 4(4), 529–544.

European Space Agency. (2015) *Sentinel-2 user handbook (1.2)*. Available at: https://sentinel.esa.int/documents/247904/685211/Sentinel-2_User_Handbook [Accessed May 24th, 2021].

Fausto, R.S., van As, D., Box, J.E., Colgan, W. and Langen, P.L. (2016a) Quantifying the surface energy fluxes in South Greenland during the 2012 high melt episodes using In-situ observations. *Frontiers in Earth Science*, 4, 82.

Fausto, R.S., van As, D., Box, J.E., Colgan, W., Langen, P.L. and Mottram, R.H. (2016b) The implication of nonradiative energy fluxes dominating Greenland ice sheet exceptional ablation area surface melt in 2012. *Geophysical Research Letters*, 43(6), 2649–2658.

Fausto, R.S., van As, D., Mankoff, K.D., Vandecrux, B., Citterio, M., Ahlstrøm, A.P., Andersen, S.B., Colgan, W., Karlsson, N.B., Kjeldsen, K.K., Korsgaard, N.J., Larsen, S.H., Nielsen, S., Pedersen, A.Ø., Shields, C.L., Solgaard, A.M. and Box, J.E. (2021) Programme for monitoring of the Greenland ice sheet (PROMICE) automatic weather station data. *Earth System Science Data*, 13(8), 3819–3845.

Flato, G., Marotzke, J., Abiodun, B., Braconnot, P., Chou, S.C., Collins, W., et al. (2013) Evaluation of climate models. In: Stocker, T.F., Qin, D., Plattner, G.-K., Tignor, M., Allen, S.K., Boschung, J., et al. (Eds.) *Climate Change 2013: The Physical Science Basis. Contribution of Working Group I to the Fifth Assessment Report of the Intergovernmental Panel on Climate Change*. Cambridge, United Kingdom, New York, NY, USA: Cambridge University Press, pp. 741–866.

Forster, P., Storelvmo, T., Armour, K., Collins, W., Dufresne, J.L., Frame, D., et al. (2021) The Earth's energy budget, climate feedbacks, and climate sensitivity. In: Masson-Delmotte, V., Zhai, P., Pirani, A., Connors, S.L., Péan, C., Berger, S., et al. (Eds.) *Climate Change 2021: The Physical Science Basis. Contribution of Working Group I to the Sixth Assessment Report of the Intergovernmental Panel on Climate Change*. Cambridge, United Kingdom, New York, NY, USA: Cambridge University Press. In Press.

Frantz, D., Haß, E., Uhl, A., Stoffels, J. and Hill, J. (2018) Improvement of the Fmask algorithm for Sentinel-2 images: separating clouds from bright surfaces based on parallax effects. *Remote Sensing of Environment*, 215, 471–481.

Gilbert, E., Orr, A., King, J.C., Renfrew, I.A., Lachlan-Cope, T., Field, P.F. and Boutle, I.A. (2020) Summertime cloud phase strongly influences surface melting on the Larsen C ice shelf, Antarctica. *Quarterly Journal of the Royal Meteorological Society*, 146(729), 1575–1589.

Gilson, G.F., Jiskoot, H., Cassano, J.J., Gultepe, I. and James, T.D. (2018) The thermodynamic structure of Arctic coastal fog occurring during the melt season over East Greenland. *Boundary-Layer Meteorology*, 168(3), 443–467.

Golledge, N.R., Keller, E.D., Gomez, N., Naughten, K.A., Bernales, J., Trusel, L.D. and Edwards, T.L. (2019) Global environmental consequences of twenty-first-century ice-sheet melt. *Nature*, 566(7742), 65–72.

Graham, R.M., Hudson, S.R. and Maturilli, M. (2019) Improved performance of ERA5 in Arctic gateway relative to four global atmospheric Reanalyses. *Geophysical Research Letters*, 46(11), 6138–6147.

Guenther, B., Xiong, X., Salomonson, V.V., Barnes, W.L. and Young, J. (2002) On-orbit performance of the earth observing system moderate resolution imaging Spectroradiometer, first year of data. *Remote Sensing of Environment*, 83(1–2), 16–30.

Hahn, L.C., Storelvmo, T., Hofer, S., Parfitt, R. and Ummenhofer, C.C. (2020) Importance of orography for Greenland cloud and melt response to atmospheric blocking. *Journal of Climate*, 33(10), 4187–4206.

Hall, D.K., Comiso, J.C., DiGirolamo, N.E., Shuman, C.A., Box, J.E. and Koenig, L.S. (2013) Variability in the surface temperature and melt extent of the Greenland ice sheet from MODIS. *Geophysical Research Letters*, 40(10), 2114–2120.

Hines, K.M. and Bromwich, D.H. (2008) Development and testing of polar weather research and forecasting (WRF) model. Part I: Greenland ice sheet meteorology. *Monthly Weather Review*, 136(6), 1971–1989.

Hines, K.M. and Bromwich, D.H. (2017) Simulation of late summer Arctic clouds during ASCOS with polar WRF. *Monthly Weather Review*, 145(2), 521–541.

Hines, K.M., Bromwich, D.H., Bai, L.-S., Barlage, M. and Slater, A.G. (2011) Development and testing of polar WRF. Part III: Arctic land. *Journal of Climate*, 24(1), 26–48.

Hines, K.M., Bromwich, D.H., Bai, L.-S., Bitz, C.M., Powers, J.G. and Manning, K.W. (2015) Sea ice enhancements to polar WRF. *Monthly Weather Review*, 143(6), 2363–2385.

Hines, K.M., Bromwich, D.H., Wang, S.-H., Silber, I., Verlinde, J. and Lubin, D. (2019) Microphysics of summer clouds in central West Antarctica simulated by the polar weather research and forecasting model (WRF) and the Antarctic mesoscale prediction system (AMPS). *Atmospheric Chemistry and Physics*, 19(19), 12431–12454.

Hochreuther, P., Neckel, N., Reimann, N., Humbert, A. and Braun, M. (2021) Fully automated detection of supraglacial Lake area for Northeast Greenland using Sentinel-2 time-series. *Remote Sensing*, 13(2), 205.

Hofer, S., Tedstone, A.J., Fettweis, X. and Bamber, J.L. (2017) Decreasing cloud cover drives the recent mass loss on the Greenland ice sheet. *Science Advances*, 3(6), e1700584.

Holz, R.E., Ackerman, S.A., Nagle, F.W., Frey, R., Dutcher, S., Kuehn, R.E., Vaughan, M.A. and Baum, B. (2008) Global moderate resolution imaging Spectroradiometer (MODIS) cloud detection and height evaluation using CALIOP. *Journal of Geophysical Research*, 113, D00A19.

Howat, I.M., Negrete, A. and Smith, B.E. (2014) The Greenland ice mapping project (GIMP) land classification and surface elevation data sets. *The Cryosphere*, 8(4), 1509–1518.

Inoue, J., Sato, K., Rinke, A., Cassano, J.J., Fettweis, X., Heinemann, G., Matthes, H., Orr, A., Phillips, T., Seefeldt, M., Solomon, A. and Webster, S. (2021) Clouds and radiation processes in regional climate models evaluated using observations over the ice-free Arctic Ocean. *Journal of Geophysical Research-Atmospheres*, 126(1), e2020JD033904.

Intrieri, J.M. (2002) An annual cycle of Arctic surface cloud forcing at SHEBA. *Journal of Geophysical Research*, 107(C10), 8039.

Izeboud, M., Lhermitte, S., van Tricht, K., Lenaerts, J.T.M., van Lipzig, N.P.M. and Wever, N. (2020) The spatiotemporal variability of cloud radiative effects on the Greenland ice sheet surface mass balance. *Geophysical Research Letters*, 47(12), e2020GL087315.

Janjić, Z.I. (1994) The Step-Mountain eta coordinate model: further developments of the convection, viscous sublayer, and turbulence closure schemes. *Monthly Weather Review*, 122(5), 927–945.

Janjić, Z. I. (2002) Nonsingular implementation of the Mellor–Yamada level 2.5 scheme in the NCEP Meso model. Office Note 437, National Centers for Environmental Prediction, 61 pp.

Jiskoot, H., Harvey, T. and Nielsen, T.R. (2019) MODIS-derived Arctic melt season fog and low stratus over East Greenland glaciers and the ice sheet. *Canadian Journal of Remote Sensing*, 45(3–4), 386–404.

Kain, J.S. (2004) The Kain-Fritsch convective parametrization: An update. *Journal of Applied Meteorology*, 43(1), 170–181.

Kay, J.E., L′Ecuyer, T., Chepfer, H., Loeb, N., Morrison, A. and Cesana, G. (2016) Recent advances in Arctic cloud and climate research. *Current Climate Change Reports*, 2(4), 159–169.

Khan, S.A., Kjær, K.H., Bevis, M., Bamber, J.L., Wahr, J., Kjeldsen, K.K., Bjørk, A.A., Korsgaard, N.J., Stearns, L.A., van den Broeke, M.R., Liu, L., Larsen, N.K. and Muresan, I.S. (2014) Sustained mass loss of the Northeast Greenland ice sheet triggered by regional warming. *Nature Climate Change*, 4(4), 292–299.

King, M., Platnick, S., Menzel, W.P., Ackerman, S.A. and Hubanks, P.A. (2013) Spatial and temporal distribution of clouds observed by MODIS onboard the Terra and Aqua satellites. *IEEE Transactions on Geoscience and Remote Sensing*, 51(7), 3826–3852.

Kotarba, A.Z. (2020) Calibration of global MODIS cloud amount using CALIOP cloud profiles. *Atmospheric Measurement Techniques*, 13(9), 4995–5012.

Kropač, E., Mölg, T., Cullen, N.J., Collier, E., Pickler, C. and Turton, J.V. (2021) A detailed, multi-scale assessment of an Atmospheric River event and its impact on extreme glacier melt in the southern Alps of New Zealand. *Journal of Geophysical Research-Atmospheres*, 126(9), e2020JD034217.

Lacour, A., Chepfer, H., Miller, N.B., Shupe, M.D., Noel, V., Fettweis, X., Gallee, H., Kay, J.E., Guzman, R. and Cole, J. (2018) How well are clouds simulated over Greenland in climate models? Consequences for the surface cloud radiative effect over the ice sheet. *Journal of Climate*, 31(22), 9293–9312.

Lacour, A., Chepfer, H., Shupe, M.D., Miller, N.B., Noel, V., Kay, J., Turner, D.D. and Guzman, R. (2017) Greenland clouds observed in CALIPSO-GOCCP: comparison with ground-based summit observations. *Journal of Climate*, 30(15), 6065–6083.

Lee, J.Y., Marotzke, J., Bala, G., Cao, L., Corti, S., Dunne, J.P., et al. (2021) Future global climate. Scenario-based projections and near-term information. In: Masson-Delmotte, V., Zhai, P., Pirani, A., Connors, S.L., Péan, C., Berger, S., et al. (Eds.) *Climate Change 2021: The Physical Science Basis. Contribution of Working Group I to the Sixth Assessment Report of the Intergovernmental Panel on Climate Change*. Cambridge, United Kingdom, New York, NY, USA: Cambridge University Press. In Press.

Lee, S., Stroeve, J., Tsamados, M. and Khan, A.L. (2020) Machine learning approaches to retrieve pan-Arctic melt ponds from visible satellite imagery. *Remote Sensing of Environment*, 247, 111919.

Lenaerts, J.T.M., Gettelman, A., van Tricht, K., Kampenhout, L. and Miller, N.B. (2020) Impact of cloud physics on the Greenland ice sheet near-surface climate: A study with the community atmosphere model. *Journal of Geophysical Research-Atmospheres*, 125(7), e2019JD031470.

Li, J., Wu, Z., Hu, Z., Jian, C., Luo, S., Mou, L., et al. (2022) A lightweight deep learning-based cloud detection method for sentinel-2A imagery fusing multiscale spectral and spatial features. *IEEE Geoscience and Remote Sensing Letters*, 60, 1–19.

Listowski, C. and Lachlan-Cope, T. (2017) The microphysics of clouds over the Antarctic peninsula—part 2: modelling aspects within polar WRF. *Atmospheric Chemistry and Physics*, 17(17), 10195–10221.

Liu, Y., Ackerman, S.A., Maddux, B.C., Key, J.R. and Frey, R.A. (2010) Errors in cloud detection over the Arctic using a satellite imager and implications for observing feedback mechanisms. *Journal of Climate*, 23(7), 1894–1907.

Livneh, B., Xia, Y., Mitchell, K.E., Ek, M.B. and Lettenmaier, D.P. (2010) Noah LSM snow model diagnostics and enhancements. *Journal of Hydrometeorology*, 11(3), 721–738.

Manabe, S. and Stouffer, R.J. (1980) Sensitivity of a global climate model to an increase of CO 2 concentration in the atmosphere. *Journal of Geophysical Research*, 85(C10), 5529.

Mattingly, K.S., Mote, T.L., Fettweis, X., van As, D., van Tricht, K., Lhermitte, S., Pettersen, C. and Fausto, R.S. (2020) Strong summer atmospheric Rivers trigger Greenland ice sheet melt through spatially varying surface energy balance and cloud regimes. *Journal of Climate*, 33(16), 6809–6832.

Mattingly, K.S., Turton, J.V., Wille, J., Nöel, B. and Fettweis, X. (2022) Increasing northeast Greenland melt driven by atmospheric rivers and föhn winds. *Nature Communications* (submitted).

Matveeva, T. and Sidorchuk, A. (2020) Modelling of surface runoff on the Yamal peninsula, Russia, using ERA5 reanalysis. *Water*, 12(8), 2099.

Miller, N.B., Shupe, M.D., Cox, C.J., Noone, D., Persson, P.O.G. and Steffen, K. (2017) Surface energy budget responses to radiative forcing at summit, Greenland. *The Cryosphere*, 11(1), 497–516.

Miller, N.B., Shupe, M.D., Cox, C.J., Walden, V.P., Turner, D.D. and Steffen, K. (2015) Cloud radiative forcing at summit, Greenland. *Journal of Climate*, 28(15), 6267–6280.

Minnett, P.J. (1999) The influence of solar zenith angle and cloud type on cloud radiative forcing at the surface in the Arctic. *Journal of Climate*, 12(1), 147–158.

Mölg, T., Cullen, N.J., Hardy, D.R., Winkler, M. and Kaser, G. (2009) Quantifying climate change in the tropical Midtroposphere over East Africa from glacier shrinkage on Kilimanjaro. *Journal of Climate*, 22(15), 4162–4181.

Moeller, C. C., Frey, R. A., Borbas, E., Menzel, W. P., Wilson, T., Wu, A. and Geng, X. (2017) Improvements to Terra MODIS L1B, L2, and L3 science products through using crosstalk corrected L1B radiances. *Proceedings of the SPIE*, *10402*, *Earth Observing Systems* XXII (104020O), 24.

Moon, T. A., Tedesco, M., Box, J. E., Cappelen, J., Fausto, R. S., Fettweis, X. et al. (2021) Greenland ice sheet. In: *Moon*, *T. A.*, *Druckenmiller*, *M. L.*, *Thoman, R. L. (ed.): NOAA Arctic report card 2021, 23–31*.

Morrison, H., McCoy, R.B., Klein, S.A., Xie, S., Luo, Y., Avramov, A., Chen, M., Cole, J.N.S., Falk, M., Foster, M.J., del Genio, A.D., Harrington, J.Y., Hoose, C., Khairoutdinov, M.F., Larson, V.E., Liu, X., McFarquhar, G.M., Poellot, M.R., von Salzen, K., Shipway, B.J., Shupe, M.D., Sud, Y.C., Turner, D.D., Veron, D.E., Walker, G.K., Wang, Z., Wolf, A.B., Xu, K.M., Yang, F. and Zhang, G. (2009) Intercomparison of model simulations of mixed-phase clouds observed during the ARM mixed-phase Arctic cloud experiment. II: multilayer cloud. *Quarterly Journal of the Royal Meteorological Society*, 135(641), 1003–1019.

Mouginot, J., Rignot, E., Bjørk, A.A., van den Broeke, M., Millan, R., Morlighem, M., Noël, B., Scheuchl, B. and Wood, M. (2019) Forty-six years of Greenland ice sheet mass balance from 1972 to 2018. *Proceedings of the National Academy of Sciences of the United States of America*, 116(19), 9239–9244.

Mouginot, J., Rignot, E., Scheuchl, B., Fenty, I., Khazendar, A., Morlighem, M., Buzzi, A. and Paden, J. (2015) Fast retreat of Zachariæ Isstrøm, Northeast Greenland. *Science*, 350(6266), 1357–1361.

Nghiem, S.V., Hall, D.K., Mote, T.L., Tedesco, M., Albert, M.R., Keegan, K., Shuman, C.A., DiGirolamo, N.E. and Neumann, G. (2012) The extreme melt across the Greenland ice sheet in 2012. *Geophysical Research Letters*, 39(20), L20502.

Niwano, M., Hashimoto, A. and Aoki, T. (2019) Cloud-driven modulations of Greenland ice sheet surface melt. *Scientific Reports*, 9(1), 10380.

Oppenheimer, M., Glavovic, B.C., Hinkel, J., van de Wal, R., Magnan, A.K., Abd-Elgawad, A., et al. (2019) Sea level rise and implications for low-Lying Islands, coasts and Communitie. In: Pörtner, H.-O., Roberts, D.C., Masson-Delmotte, V., Zhai, P., Tignor, M., Poloczanska, E., et al. (Eds.) *IPCC Special Report on the Ocean and Cryosphere in a Changing Climate*. Cambridge, United Kingdom, New York, NY, USA: Cambridge University Press. In press, pp. 321–445.

Orsolini, Y., Wegmann, M., Dutra, E., Liu, B., Balsamo, G., Yang, K., de Rosnay, P., Zhu, C., Wang, W., Senan, R. and Arduini, G. (2019) Evaluation of snow depth and snow cover over the Tibetan plateau in global reanalyses using in situ and satellite remote sensing observations. *The Cryosphere*, 13(8), 2221–2239.

Otkin, J.A. and Greenwald, T.J. (2008) Comparison of WRF model-simulated and MODIS-derived cloud data. *Monthly Weather Review*, 136(6), 1957–1970.

Paluch, I.R., Lenschow, D.H. and Wang, Q. (1997) Arctic boundary layer in the fall season over open and frozen sea. *Journal of Geophysical Research*, 102(D22), 25955–25971.

Pedersen, S.H., Tamstorf, M.P., Abermann, J., Westergaard-Nielsen, A., Lund, M., Skov, K., Sigsgaard, C., Mylius, M.R., Hansen, B.U., Liston, G.E. and Schmidt, N.M. (2016) Spatiotemporal characteristics of seasonal snow cover in Northeast greenland from in situ observations. *Arctic, Antarctic and Alpine Research*, 48(4), 653–671.

Platnick, S., Meyer, K. G., King, M. D., Wind, G., Amarasinghe, N., Marchant, B. et al. (2018) *MODIS cloud optical properties: user guide for the collection 6/6.1 Level-2 MOD06/MYD06 product and associated Level-3 datasets. Version 1.1*. https://atmosphere-imager.gsfc.nasa.gov/sites/default/files/ModAtmo/C6MOD06OPUser Guide_0.Pdf [=Accessed June 6th, 2021].

Qiu, S., Zhu, Z. and He, B. (2019) Fmask 4.0: improved cloud and cloud shadow detection in Landsats 4–8 and Sentinel-2 imagery. *Remote Sensing of Environment*, 231, 111205.

Rantanen, M., Karpechko, A.Y., Lipponen, A., Nordling, K., Hyvärinen, O., Ruosteenoja, K., Vihma, T. and Laaksonen, A. (2022) The Arctic has warmed nearly four times faster than the globe since 1979. *Communications Earth & Environment*, 3, 168.

Rasmussen, L.H., Zhang, W., Hollesen, J., Cable, S., Christiansen, H.H., Jansson, P.-E. and Elberling, B. (2018) Modelling present and future permafrost thermal regimes in Northeast Greenland. *Cold Regions Science and Technology*, 146, 199–213.

Reynolds, R.W., Smith, T.M., Liu, C., Chelton, D.B., Casey, K.S. and Schlax, M.G. (2007) Daily high-resolution-blended analyses for sea surface temperature. *Journal of Climate*, 20(22), 5473–5496.

Rignot, E. and Kanagaratnam, P. (2006) Changes in the velocity structure of the Greenland ice sheet. *Science*, 311(5763), 986–990.

Ruan, R., Chen, X., Zhao, J., Perrie, W., Mottram, R., Zhang, M., Diao, Y., du, L. and Wu, L. (2019) Decelerated Greenland ice sheet melt driven by positive summer North Atlantic oscillation. *Journal of Geophysical Research-Atmospheres*, 124(14), 7633–7646.

Sasgen, I., Wouters, B., Gardner, A.S., King, M.D., Tedesco, M., Landerer, F.W., Dahle, C., Save, H. and Fettweis, X. (2020) Return to rapid ice loss in Greenland and record loss in 2019 detected by the GRACE-FO satellites. *Communications Earth Environment*, 1, 8.

Sedlar, J., Tjernström, M., Rinke, A., Orr, A., Cassano, J., Fettweis, X., Heinemann, G., Seefeldt, M., Solomon, A., Matthes, H., Phillips, T. and Webster, S. (2020) Confronting Arctic troposphere, clouds, and surface energy budget representations in regional climate models with observations. *Journal of Geophysical Research-Atmospheres*, 125(6), e2019JD031783.

Serreze, M.C. and Meier, W.N. (2019) The Arctic′s sea ice cover: trends, variability, predictability, and comparisons to the Antarctic. *Annals of the New York Academy of Sciences*, 1436(1), 36–53.

Shupe, M.D. and Intrieri, J.M. (2004) Cloud radiative forcing of the Arctic surface: the influence of cloud properties, surface albedo, and solar zenith angle. *Journal of Climate*, 17(3), 616–628.

Skamarock, W.C., Klemp, J.B., Dudhia, J., Gill, D.O., Liu, Z., Berner, J., et al. (2019) *A Description of the Advanced Research WRF Model Version 4. NCAR Tech. Note NCAR/TN-556+STR*. Boulder, Calorado: UCAR/NCAR.

Sneed, W.A. and Hamilton, G.S. (2016) Recent changes in the Norske Øer ice barrier, coastal Northeast Greenland. *Annals of Glaciology*, 57(73), 47–55.

Solomon, A., Shupe, M.D. and Miller, N.B. (2017) Cloud–atmospheric boundary layer–surface interactions on the Greenland ice sheet during the July 2012 extreme melt event. *Journal of Climate*, 30(9), 3237–3252.

Sotiropoulou, G., Vignon, É., Young, G., Morrison, H., O'Shea, S.J., Lachlan-Cope, T., et al. (2021) Secondary ice production in summer clouds over the Antarctic coast: an underappreciated process in atmospheric models. *Atmospheric Chemistry and Physics*, 21(2), 755–771.

Tan, S., Zhang, X. and Shi, G. (2019) MODIS cloud detection evaluation using CALIOP over polluted eastern China. *Atmosphere*, 10(6), 333.

Tarrio, K., Tang, X., Masek, J.G., Claverie, M., Ju, J., Qiu, S., Zhu, Z. and Woodcock, C.E. (2020) Comparison of cloud detection algorithms for Sentinel-2 imagery. *Science of Remote Sensing*, 2, 100010.

Tedesco, M. and Fettweis, X. (2020) Unprecedented atmospheric conditions (1948–2019) drive the 2019 exceptional melting season over the Greenland ice sheet. *The Cryosphere*, 14(4), 1209–1223.

Temme, F., Turton, J.V., Mölg, T. and Sauter, T. (2020) Flow regimes and Föhn types characterize the local climate of southern Patagonia. *Atmosphere*, 11(9), 899.

The IMBIE Team. (2020) Mass balance of the Greenland ice sheet from 1992 to 2018. *Nature*, 579(7798), 233–239.

Tjernström, M., Birch, C.E., Brooks, I.M., Shupe, M.D., Persson, P.O.G., Sedlar, J., Mauritsen, T., Leck, C., Paatero, J., Szczodrak, M. and Wheeler, C.R. (2012) Meteorological conditions in the Central Arctic summer during the Arctic summer Cloud Ocean study (ASCOS). *Atmospheric Chemistry and Physics*, 12(15), 6863–6889.

Turton, J.V., Hochreuther, P., Reimann, N. and Blau, M.T. (2021) The distribution and evolution of supraglacial lakes on 79° N glacier (North-Eastern Greenland) and interannual climatic controls. *The Cryosphere*, 15(8), 3877–3896.

Turton, J.V., Mölg, T. and Collier, E. (2020) High-resolution (1 km) polar WRF output for 79° N glacier and the northeast of Greenland from 2014 to 2018. *Earth System Science Data*, 12(2), 1191–1202.

Turton, J.V., Mölg, T. and van As, D. (2019) Atmospheric processes and climatological characteristics of the 79N glacier (Northeast Greenland). *Monthly Weather Review*, 147(4), 1375–1394.

van As, D., Hubbard, A.L., Hasholt, B., Mikkelsen, A.B., van den Broeke, M.R. and Fausto, R.S. (2012) Large surface meltwater discharge from the Kangerlussuaq sector of the Greenland ice sheet during the record-warm year 2010 explained by detailed energy balance observations. *The Cryosphere*, 6(1), 199–209.

van den Broeke, M. R., Box, J., Fettweis, X., Hanna, E., Noël, B., Tedesco, M. et al. (2017) Greenland ice sheet surface mass loss: recent developments in observation and modeling. *Current Climate Change Reports*, 3(4), 345–356.

van den Broeke, M.R., Enderlin, E.M., Howat, I.M., Kuipers Munneke, P., Noël, B.P.Y., van de Berg, W.J., van Meijgaard, E. and Wouters, B. (2016) On the recent contribution of the Greenland ice sheet to sea level change. *The Cryosphere*, 10(5), 1933–1946.

van den Broeke, M.R., Smeets, P., Ettema, J. and Munneke, P.K. (2008) Surface radiation balance in the ablation zone of the West Greenland ice sheet. *Journal of Geophysical Research*, 113(D13), D13105.

van Tricht, K., Lhermitte, S., Lenaerts, J.T.M., Gorodetskaya, I.V., L'Ecuyer, T.S., Noël, B., van den Broeke, M.R., Turner, D.D. and van Lipzig, N.P.M. (2016) Clouds enhance Greenland ice sheet meltwater runoff. *Nature Communications*, 7, 10266.

Velicogna, I. and Wahr, J. (2006) Acceleration of Greenland ice mass loss in spring 2004. *Nature*, 443(7109), 329–331.

Vignon, É., Besic, N., Jullien, N., Gehring, J. and Berne, A. (2019) Microphysics of snowfall over coastal East Antarctica simulated by polar WRF and observed by radar. *Journal of Geophysical Research-Atmospheres*, 124(21), 11452–11476.

Vihma, T., Screen, J., Tjernström, M., Newton, B., Zhang, X., Popova, V., Deser, C., Holland, M. and Prowse, T. (2016) The atmospheric role in the Arctic water cycle: A review on processes, past and future changes, and their impacts. *Journal of Geophysical Research. Biogeosciences*, 121(3), 586–620.

Wang, W., Zender, C.S. and van As, D. (2018) Temporal characteristics of cloud radiative effects on the Greenland ice sheet: discoveries from multiyear automatic Weather Station measurements. *Journal of Geophysical Research-Atmospheres*, 123(11), 11,348–11,361.

Wang, W., Zender, C.S., van As, D. and Miller, N.B. (2019) Spatial distribution of melt-season cloud radiative effects over Greenland: evaluating satellite observations, reanalyses, and model simulations against in situ measurements. *Journal of Geophysical Research-Atmospheres*, 124(1), 57–71.

Wang, X., Tolksdorf, V., Otto, M. and Scherer, D. (2021) WRF-based dynamical downscaling of ERA5 reanalysis data for High Mountain Asia: towards a new version of the high Asia refined analysis. *International Journal of Climatology*, 41(1), 743–762.

Ward, J.L., Flanner, M.G. and Dunn-Sigouin, E. (2020) Impacts of Greenland block location on clouds and surface energy fluxes over the Greenland ice sheet. *Journal of Geophysical Research-Atmospheres*, 125(22), e2020JD033172.

Wilks, D.S. (2011) *Statistical Methods in the Atmospheric Sciences*, 3rd edition. Amsterdam: Elsevier/Academic Press (International geophysics series, p. 100.

Wilson, A.B., Bromwich, D.H. and Hines, K.M. (2011) Evaluation of polar WRF forecasts on the Arctic system reanalysis domain: surface and upper air analysis. *Journal of Geophysical Research*, 116(D11), D11112.

Wilson, A.B., Bromwich, D.H. and Hines, K.M. (2012) Evaluation of polar WRF forecasts on the Arctic system reanalysis domain: 2. Atmospheric hydrologic cycle. *Journal of Geophysical Research*, 117(D4), D04107.

Zekoll, V., Main-Knorn, M., Alonso, K., Louis, J., Frantz, D., Richter, R. and Pflug, B. (2021) Comparison of masking algorithms for Sentinel-2 imagery. *Remote Sensing*, 13(1), 137.

Zhang, B., Liu, L., Khan, S.A., van Dam, T., Bjørk, A.A., Peings, Y., Zhang, E., Bevis, M., Yao, Y. and Noël, B. (2019) Geodetic and model data reveal different spatio-temporal patterns of transient mass changes over Greenland from 2007 to 2017. *Earth and Planetary Science Letters*, 515, 154–163.

Zhang, T., Stamnes, K. and Bowling, S.A. (1996) Impact of clouds on surface radiative fluxes and snowmelt in the Arctic and subarctic. *Journal of Climate*, 9(9), 2110–2123.

Zhu, X. and Helmer, E.H. (2018) An automatic method for screening clouds and cloud shadows in optical satellite image time series in cloudy regions. *Remote Sensing of Environment*, 214, 135–153.

Zhu, Z., Wang, S. and Woodcock, C.E. (2015) Improvement and expansion of the Fmask algorithm: cloud, cloud shadow, and snow detection for Landsats 4–7, 8, and sentinel 2 images. *Remote Sensing of Environment*, 159, 269–277.

Zhu, Z. and Woodcock, C.E. (2012) Object-based cloud and cloud shadow detection in Landsat imagery. *Remote Sensing of Environment*, 118, 83–94.

How to cite this article: Andernach, M., Turton, J.V. & Mölg, T. (2022) Modeling cloud properties over the 79 N Glacier (Nioghalvfjerdsfjorden, NE Greenland) for an intense summer melt period in 2019. *Quarterly Journal of the Royal Meteorological Society*, 148(749), 3566–3590. Available from: https://doi.org/10.1002/qj.4374